9950-1026

ANALYSIS OF THE GRAN DESIERTO - PINACATE REGION, SONORA, MEXICO, VIA SHUTTLE IMAGING RADAR

by

Ronald Greeley, Philip R. Christensen, John F. McHone,

Yemane Asmerom, and James R. Zimbelman

Department of Geology
Arizona State University
Tempe, AZ 85287

1984

Contract No. NSG-7289

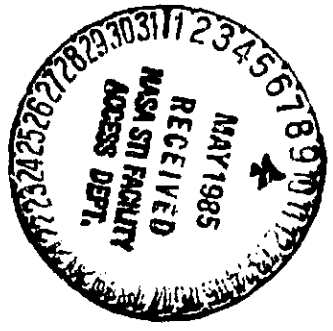

ANALYSIS OF THE GRAN DESIERTO - PINACATE REGION, SONORA, MEXICO, VIA SHUTTLE IMAGING RADAR

1.0 Introduction

Radar imaging techniques were developed during the 1950s primarily for military objectives. Geological applications began with declassification of some imaging systems during the mid-to-late 1960s and advanced as several commercial organizations made radar images available during the 1970s. During this time, the advantages of radar as a remote sensing technique for recognizing geological features such as faults and other linear structures became apparent. Fundamentals of radar imaging and its application in geology are discussed in most current textbooks on remote sensing and image interpretation (e.g., Sabins, 1978; and Siegel and Gillespie, 1980).

The first civilian orbital radar images were produced in 1978 by the Seasat mission (Born et al., 1979). Although this mission was originally designed to obtain information on oceanic features such as wave forms and sea ice, radar images acquired over a few land areas revealed a potential for geological applications (Ford et al., 1980). Partly due to these promising results, the Shuttle Imaging Radar (SIR) experiment was proposed, designed, and subsequently flown in 1981. Preliminary results from the first SIR mission (SIR-A) have been reported by Elachi et al. (1982) and others.

Radar imaging is also important in space exploration. A high priority in Solar System exploration, detailed surface observations of cloud-covered Venus will become possible only with radar systems carried on orbiting spacecraft. Initially proposed as Venus Orbiting Imaging Radar (VOIR) in the late 1970s, such a mission has been redesigned as the Venus Radar Mapper (VRM), to be flown in the late 1980s. This exploratory mission will characterize surface features on Venus and produce a global radar map with a spatial resolution of

about 1 km. Although not yet a funded mission, current NASA plans (SSEC, 1983) call for a similar radar system to map the surface of Titan, largest satellite of Saturn and the only satellite known to have a substantial atmosphere and clouds.

The study reported here is part of a general investigation to determine radar discriminability of aeolian features and their geological setting as imaged by the SIR-A experiment. This report focuses on the the Gran Desierto and Pinacate volcanic field of Sonora in northern Mexico (Fig. 1) with objectives of analyzing radar characteristics of the interplay of aeolian features and volcanic terrain. The study area in the Gran Desierto covers some 4000 km^2 and contains sand dunes of several forms, as reviewed briefly by Smith (1982) and by Blom and Elachi (1981) in their assessment of radar signatures for sand dunes. The Pinacate volcanic field covers more than 2,000 km^2 (Gutmann, 1979) and consists primarily of basaltic lavas. Margins of the field, especially on the western and northern sides, include several maar and maar-like craters; thus, a secondary objective of our study was to obtain information on their radar characteristics for comparison with impact craters.

1.1 Data Characteristics

The SIR-A experiment was flown aboard the test flight of Space Shuttle Columbia in November, 1981 (Settle and Taranik, 1982). The experiment involved a side-looking, synthetic aperture, horizontally polarized, microwave radiation system transmitting and receiving an L-band frequency (23.5 cm wavelength) beam at an incidence angle of 50 ± 3° from vertical. During the shuttle flight, the system operated for a total time of about 8 hours, acquiring images for approximately 10 million km^2 with a ground resolution of about 40 m. Ground coverage consisted of a 50 km wide strip paralleling

the northern side of the spacecraft orbit and extending across entire continents.

Preliminary science analyses of SIR-A images are given by Elachi et al. (1982) and in other papers of the 3 December 1983 issue of Science, and by Ford et al. (1983). McCauley et al. (1982) include a discussion of SIR-A images of desert and aeolian terrains.

Images used in this study are listed in Table 1. SIR-A coverage (Fig. 2a) over the study site was acquired 13 November 1981 during Data Take 24-C and covers approximately 6,000 km^2. Seasat images obtained in September 1978 were used for comparison. The instrument used on Seasat was a predecessor of the SIR-A and was also a side-looking, horizontally polarized synthetic aperture system operating at 23.5 cm wavelength, differing from SIR-A primarily in its incidence angle of 20°. In addition to radar images, orbital Skylab photographs (Fig. 3) were used for synoptic views. These true color photographs were used to delineate major surface features on both the aeolian terrain and the volcanic field. Conventional vertical aerial photographs (~1:85,000) available from DETENAL (Direccion General de Estudios del Territorio Nacional, Mexico) were used for detailed photogeologic interpretations. DETENAL maps (1:50,000) were used for orientation and topographic detail. Because place names in the Pinacate area are not uniform in all publications (Table 2), we have used those of Donnelly (1974).

1.2 Method of Study

Our study consisted of three phases: laboratory analysis, aerial reconnaissance, and field work. Laboratory analysis involved photogeological mapping and interpretation of Skylab and conventional aerial photographs for comparison with radar "units" derived from the SIR-A image. Dune forms and other aeolian features were identified and delineated in Gran Desierto. Lava

flow surface textures and morphology of the Pinacate field were mapped and compared with field results of Donnelly (1974) and Lynch (1981).

Targets of specific interest were identified from photogeological analyses for additional study and for subsequent aerial reconnaissance. On 19 February 1983 an aerial reconnaissance flight was made over the study area to obtain high resolution, low altitude photographs and to observe selected sites. For example, some radar-bright areas were identified as blocky crater rims, whereas some radar-dark areas were observed to be sandy plains. In addition, some relatively inaccessable sites of interest in the dune fields and in the interior of the Pinacate field, which were unlikely to be visited on the ground, were observed at low altitude from the air. Results from the aerial reconnaissance are described in Section 3.

On 12-15 February 1983 a preliminary field trip was carried out by one of us (PC) to determine ground accessibility of the western margin of the Pinacate field and potential methods for assessing surface characteristics for detailed field study. On 15 April 1983 a field party from the ASU Planetary Geology Group travelled to the western margin of Pinacate for a five-day field excursion. A second field excursion was conducted in December, 1983 to investigate the eastern margin of the lava field and the summit area of Pinacate. During these trips specific sites identified by the laboratory study and the aerial reconnaissance were examined to assess radar characteristics and surface textures, as described in Section 4.

2.0 General Geology

2.1 Previous Investigations

As early as 1701, the Jesuit missionary Padre Kino recognized lavas in the Pinacate Mountains of Sonora (Fig. 4), thus establishing the first identified volcanic field in North America. Explorers two centuries later

wrote of several large volcanic craters on the northern flanks of the field (MacDougal, 1908; Hornaday, 1908; Lumholtz, 1912). In 1929 the parts of the shield which extend northward across the US-Mexico border were mapped by Wilson (1933). Jahns and Fielder (1952) first suggested a collapse origin for the large craters and Jahns (1959) prepared the first detailed geologic maps of the area. Geology of the volcanic craters, cones, and lava flows in the Pinacate field have been described by Donnelly (1974), Gutmann (1972, 1976, 1977, 1979), and Gutmann and Sheridan (1978). The genesis and ages of the volcanism were described by Lynch (1981). May (1973) provided reconnaissance mapping of the Gran Desierto region, and Blom (1983) presented a brief discussion of the Pinacate field and adjacent dunes and compared their appearance on Shuttle Imaging Radar and Landsat images.

Sand deposits south and west of the Pinacates were studied by Merriam and Bandy (1965) and Merriam (1969), who concluded that the sands were derived from Colorado River sediments. Arvidson and Mutch (1974) suggested that windblown sands were being transported northward around the margin of the volcano field but that the sediments filling crater floors were derived locally from lavas, tuffs, and tuff breccias. McKee et al. (1976, 1977) and Breed and Grow (1979) described the distribution and morphology of dunes in the area from their analyses of Landsat and Skylab images. Blom and Elachi (1981) studied the dunes on Seasat orbital radar images. Smith (1982) briefly discussed the Gran Desierto in his review of North American sand dunes.

2.2 Regional Setting

The general geology of the area has been described by Ives (1949, 1964), Jahns (1959), Donnelly (1974), and Lynch (1981) (Fig. 2b). The Pinacate volcanic field is a broad, complex basaltic shield (Fig. 4) surrounded by NW trending outcrops of pre-Cenozoic crystalline rock and pre-Miocene volcanics and whose summit reaches 1.3 km above sea level. Oldest rocks are Precambrian

(1.6 b.y.) metasediments (Damon, 1970). During the Mesozoic and early Tertiary, granites and granodiorites associated with Laramide magmatism were emplaced and yield potassium-argon dates of 51 to 69 million years (Damon, 1970). Mesozoic to Tertiary volcanic rocks with a total thickness of 1500 m crop out southwest of the Pinacate field. Younger basaltic and andesitic lava flows as thick as 900 m occur at several locations around the margin of the field. Large-scale faulting, associated with development of the Basin and Range province, began in mid-Tertiary and formed a series of NW-SE trending fault blocks. Sedimentary rocks ranging in thickness from 600 to 900 m occur around the margin of the Pinacate field and are considered to be derived from erosion of uplifted fault blocks during this period (Kovach et al., 1962; Wood, 1974). The dune fields south and west of the Pinacates are underlain by ~900 m of sediments.

2.3 Pinacate Volcano Field

Most of the older, visible flows in the Pinacates are Quaternary basalts which closely resemble the composition of the younger lavas of the main shield. There are, however, some textural differences between the early Quaternary basalts and the later flows. An absence of magnetic reversals in the earlier Quaternary basalts implies that these rocks are younger than 17 million years old. Faulting during late Tertiary to early Quaternary uplifted segments of these flows several hundred meters and is responsible for most of the EW topographic features observed peripheral to the Pinacates, including scattered mesas that are interpreted as faulted remnants of formerly extensive lava flows. These mesas have been uplifted 45 to 900 m and display eight to ten km of horizontal offset. Eruption of the main Pinacate shield basalts occurred after this episode of faulting and only a few small faults are found within the present volcano field.

Ages of various Pinacate lavas are based on a variety of techniques. Lacustrine travertine samples from a former lake within the large, maar-like crater Elegante (Fig. 2a located at V 6) have been dated at about 17,000 years using radiocarbon techniques (Damon et al., 1963). Ninety five percent of the flows exposed on the shield are stratigraphically lower, and thus older, than these lacustrine beds. Based on estimated rates of effusion, Donnelly (1974) suggests that the Pinacate shield lavas are Pleistocene to late Holocene in age with the oldest exposed flows being 246,000 to 327,000 years old. The most recent volcanic activity in the area is associated with a few small cinder cones on the NE slope which, from Indian legends and early Spanish accounts, were active 300 to 1,200 years ago.

Originally, shield-forming flows erupted from five NS trending vents which eventually formed three separate shield structures (Fig. 2b). The longest flows (up to 15 km long) are found in the southernmost shield complex. Typically, they are slender tongue-like units situated on relatively steep slopes of about 10°. Shorter, ponded flows, averaging less than 5 km long, occur on the central and northern shields which have slopes of 3° to 5°. All shield flow units range in thickness from 1 to 10 m, typical of Hawaiian shield volcanoes. The formation of the shields appears to be structurally controlled by pre-existing Basin and Range tectonic elements. Magmas related to the east Pacific rise may have migrated upward along EW-trending transform fault fractures formed during the opening of the Gulf of California (Larson et al., 1968; Lipman et al., 1970). Eruptions may have occurred when ascending magma intersected older, NW-SE trending faults.

Pinacate volcanic rocks have an estimated volume of 240-290 km^3 of hawaiite flows and about 13 km^3 of pyroclastic detritus. Of the more than 650 individual lava flows mapped by Donnelly (1974), 95% are aa and 5% are

pahoehoe; 15% of the surface area is covered by more than 502 cinder and agglutinate cones which have 25° to 30° slopes and heights ranging from 12 to 120 m. Thin, unconsolidated coarse-to-fine ash and basaltic lapillae mantle much of the shield.

Nine large maar or maar-like craters (Fig. 5) and one lava-filled tuff ring are distributed around the margins of the volcanic field. Eight of these craters are in a NW-trending arcuate belt through the northern half of the northernmost shield. All craters occur at elevations below 340 m and most are below 300 m. They are 0.6 to 1.5 km in diameter, 30 to 250 m deep, and are rimmed by remnant tuff rings 8 to 30 m above the surrounding surface. Outer slopes range from 5° to 33° but are typically less than 10°. Most of the craters appear to be phreatic or phreatomagmatic explosion craters (maars) enlarged by post-explosion collapse (Jahns and Fielder, 1952; Gutmann, 1972). Criteria for collapse include a lack of rupture structures in crater walls and rims, volumes of pyroclastic ejecta that are significantly smaller than void volumes of the craters, and a predominance of juvenile ejecta rather than accessory or accidental materials in surrounding pyroclastic rings. Donnelly (1974) used the terms explosion-collapse craters and compound craters to further stress the role of slumping and collapse in the final morphology and structure of these craters. At several locations, pre-existing lava flows, dikes, and even cinder cones are exposed in crater walls beneath the present uppermost rim of tuffs and breccias (Guttman, 1979).

Formation of the craters was one of the latest volcanic events in the Pinacate field. The largest, Crater Elegante, must be older than the 17,000 year old carbonate lake beds superimposed on its inner slopes (Damon et al., 1963). The least eroded crater, Cerro Colorado, has much of its tuff cone still intact. Pottery shards from cultures known to be in the region some

12,000 years ago were found in ejecta materials and associated alluvial outwash fans at the crater (Ives, 1956).

2.4 Gran Desierto

The largest active dune field in North America lies near the northern shore of the Gulf of California in the Gran Desierto, a subdivision of the Sonoran Desert of Mexico and the United States. Brown (1923) and Norris and Norris (1961) suggested that sands of the Gran Desierto originated from ancient Lake Cahuilla along the southeast shore of the present Salton Sea. Reconnaissance studies in the Gran Desierto (Ives, 1959; Merriam, 1969) show two zones of compositionally different sands: 1) a northern zone with granulometric and mineral affinities to fluvial sands of the present Colorado River and its deltaic deposits and 2) a southern zone rich in marine bioclastic sediments derived from the Gulf of California. Mineral compositions and microfossils from the northern Gran Desierto dune sands closely resemble sands from the Algodones Dunes of California (Merriam, 1969). In addition, similar characteristics appear in Cenozoic sediments of the Colorado River but not in the Gulf of California nor Lake Cahuilla beach sands. Merriam concluded that Cenozoic river sands transported from as far away as the Colorado Plateau were the sources for both the Californian and the northern Gran Desierto dune sands.

Style and distribution of major dune types in the Gran Desierto have been derived from aerial and satellite surveys (McKee et al., 1976, 1977; Breed and Grow, 1979; Blom and Elachi, 1981). The largest dunes are of three types, star dunes, barchanoid dunes, and linear dunes, which merge with each other in a systematic pattern. Rows of giant, 100 m high star dunes dominate the NW portion of the field in linear arrays two km apart and oriented N 60°W. These arrays grade eastward into patterns of complex crescentic (barchanoid) dunes

crested by smaller star dunes. Farther eastward and to the south of the Pinacate field, the dunes merge into large compound crescentic dunes with north-facing slip faces. Northward from the main body of complex barchanoid dunes, the sand bodies form a long narrow zone of stabilized linear dunes which trend northeastward, paralleling the northwest margin of the Pinacate volcano field. A similar field of linear dunes occurs along the eastern side of the volcanic shield (Fig. 3, *Y 5-6*). Southwest of the Pinacates along the Gulf of California shoreline, linear dunes trend northward and merge into the main mass of barchanoid dunes.

3.0 Overflight

The Pinacate-Gran Desierto study area was overflown with a fixed-wing airplane for a regional comparison of the radar reflectance properties and surface characteristics. This reconnaissance study provided observations at a scale intermediate between satellite images and ground observations and was also used to study specific regions of distinctive SIR-A radar signatures. In addition, the overflight observations were used to select sites for detailed field study (Section 4). The flight path covered a wide range of terrain types, from which six categories with distinct radar reflectance properties have been identified: 1) dune, interdune and sand-sheet surfaces, 2) washes and alluvium, 3) volcanic-sand boundaries, 4) lava flows and pyroclastics, 5) maars and cinder cones, and 6) structural features.

3.1 Gran Desierto Aeolian Surfaces

The extensive windblown deposits of the Gran Desierto produced the lowest radar return observed in the test area; there are, however, some tonal variations observed on the SIR-A radar image. These include linear patterns similar to the dune morphology and radar bright points in the vicinity of major star dune fields (Figs. 2,3 *C 9*).

Seasat and Skylab images show complex rows of star dunes southwest of the Sierra del Rosario and a smaller area of similar dunes immediately NE of this same range (Fig. 6). These smaller dunes are not as obvious on the SIR-A image, although there are numerous bright points in the vicinity of the star dunes (Fig. 6c). These localized points of strong radar return may be due to multiple reflections of the radar beam from the arms of large star dunes. In many star dunes, the steeply sloped (~30°) ridges of several arms coalesce to form large, deep depressions. These depressions may act as corner reflectors to produce small-scale, yet intense, radar returns, resulting in the pattern of bright point reflections seen in the SIR-A image.

The overall differences in radar return and dune discernability observed by the Seasat and SIR-A instruments are probably due to the 30° difference in incidence angle between the two radar systems. At Seasat viewing geometry (20° incidence) dune slip faces oriented normal to the radar beam can produce a specular return (Blom and Elachi, 1981). However, at the 50° incidence angle of SIR-A the slip faces are all less than that required to produce a bright specular return and the low incidence angle of Seasat appears to be better suited for detecting dunes. The SIR-A data provide information about the location of dune forms, but is best used in conjunction with other types of images. These data do show subtle tonal variations in some dune areas (Fig. 2a *M ?*) which may be due to differences in surface roughness between dune and interdune surfaces.

Some of the morphological features of star dunes which may be important for radar imaging are shown in Figure 7. The star dunes occur in rows which are separated by interdune areas of compound transverse dunes having lower topographic relief (Fig. 7a). Individual star dunes have three to six arm-like extensions that are generally curved in a clockwise direction (Fig.

7b). Each arm typically consists of a moderate (~15°) lower slope with a steep (~30°) upper slope leading to a sharply defined ridge crest. Small bushes, spaced approximately 10 m apart, cover the interdune areas and lower dune flanks, but are absent on the more steeply inclined active arm crests (Fig. 7c). Regions between large star dunes are also covered by sand, with transverse bedforms which have few sharp crests and appear primarily as gentle undulations. Vegetation is more closely spaced (~5 m) in the depressions of these transverse bedforms. Boulders and cobbles are absent from both the dune and interdune surfaces.

Compound barchanoid dunes occur south and southwest of the volcanic field (Fig. 8). These dunes also have very low SIR-A returns. Slip faces are approximately parallel to the SIR-A range direction; however, they face away from the radar and should not produce an enhanced return (Blom, 1983). Superimposed on the large dunes are smaller (~5-10 m high) compound transverse dunes that cover much of the dune and interdune surfaces. Medium-sized (~1 m) bushes moderately scattered over the sand surface have a slightly higher density in the interdune areas. As in the star dune field, the interdune surfaces are also covered with active sand, rather than lag or armored deposits of coarser material. Therefore, the slight differences in radar return are considered to be due to variations in surface texture, rather than particle size.

Major sand transport appears to be northward toward the volcanic field, consistent with the orientation of major slip faces. However, orientation of sand drifts on the southern side of individual bushes provides some evidence for recent sand movement to the south, at least when the observations were made. Reversing winds may play an important role in the formation of the star dunes and transverse ridges. In addition, orientation of the active slip

faces and smaller bedforms, such as ripples, at the time a radar image is acquired, may be important for determining the exact response of the surface to an incident radar beam. These effects will be especially important at lower radar incidence angles, where local slopes more strongly affect the radar reflectance.

The lack of steep (>40°) slopes, trees, and exposed rocks within the dune field are all consistent with the low SIR-A radar returns. The star dunes may produce bright corner reflections, but most of the tonal variations are likely due to sub-meter surface roughness. Used in conjunction with the Seasat data, the SIR-A images can be used to discriminate between slope and roughness effe[illegible].

3.2 Washes and Alluvium

SIR-A images clearly define drainage patterns which appear as linear features with very high radar return within the sand and volcanic fields. These features are randomly oriented with no apparent variation in radar brightness, indicating that viewing geometry plays only a slight role in radar return intensity, with the high density of radar reflectors, such as trees and boulders in the washes, being more important.

One major drainage network on the south slope of Pinacate appears as a series of bright, roughly parallel, narrow linear features perpendicular to the margin of the volcanic field (Fig. 2a *T-V 10*; and Fig. 9a). From the air these washes have significantly more vegetation than the surrounding terrain (Fig. 8). Ground inspection revealed large boulders and bedrock outcrops on many channel floors.

A second radar bright drainage system is shown in Figures 9b and 10 (Fig. 2 *L-O 6*). Widths of the washes vary from one to ten meters and vegetation is often absent along the sand floors but is frequent along the sides. Larger

bushes and trees ranging in height from 2-3 m are typically spaced 10-15 m along the washes, but are absent from the surrounding terrain. Small boulders and large cobbles are scattered throughout the washes. The braided stream in Figure 10b has large trees and brush separated by 2-4 m and separates two areas of sharp tonal contrast on aerial photography. This contrast is apparent on the SIR-A image and may be due to variations in surface roughness.

Along the SW boundary between the volcanic and aeolian terrains there is a 5-20 m wide wash into which many of the radar-bright streams flow. This wash is not apparent on the SIR-A image. Vegetation height and density is less than that found in radar-bright washes and is comparable to that in surrounding sand areas. There is little topographic relief and blocky cobbles or boulders are not present. Apparently, the low density of vegetation and lack of large rocks results in low radar return.

From these observations, washes appear to be strong radar reflectors when large trees and boulders are present, provided their spacing is less than ~15-20 m. Washes not having rocks and large vegetation within rough (radar-bright) flow units are less distinct due to the lower contrast in radar image return.

3.3 Volcanic-Sand Boundaries

The SIR-A image shows a distinct boundary between the volcanic and aeolian terrains. Volcanic surfaces are typically radar-bright, as compared to the very low radar return from aeolian deposits. The width of the transition region from radar-dark to radar-bright surfaces is variable, with the southern boundary being the most pronounced (Fig. 2a *V-W 10*).

Figure 11 shows representative aerial views of the southern margin of the volcanic field and variations in the width of the radar boundary. The margin at the southeast edge has the sharpest radar and visual boundary (Fig. 2a *V-W 10*, and Fig. 11a) where the flow is only slightly mantled and lava flow features are

visible at the boundary with the sand. Farther west the boundary is less distinct (Fig. 2a *U 10*, and Fig. 11b). The lava flow appears mantled with dark (basaltic?) particles which have buried primary flow features. Like the aeolian sand, this mantle also appears radar-dark, making the boundary between aeolian and fluvial sediments less distinct. On the southwestern margin of the field the boundary is even less sharply defined (Fig. 2a *S 9*, and Fig. 11c). Aeolian sediments cover the lava flow as a gradually thinning mantle.

3.4 Lava Flows

A wide variety of lava flow surface textures occur within the Pinacate field and display a wide range of radar and visual reflectances (Figs. 12 and 13). The youngest flows generally appear dark on the Skylab photograph and bright in the radar image (Blom, 1982). Older flows that are weathered and mantled by sediments have a range of gray tones on the photographs, with the brightest regions occurring around the margin of the field, corresponding to younger flows.

The aa flow shown in Figure 13a is one of the radar-brightest regions in the study area and appears to be relatively fresh, very blocky, and not mantled by fine material. The flow in Figure 13b is more dissected and is partly covered by sediments. The increased mantling is seen in the radar image as a mottled gray and is less bright than the aa flow. Figure 13c shows a heavily weathered and mantled flow which has a very low radar return. Compared to the aa flow (Fig. 13a), this flow has fewer bedrock ridges and exposed blocks. Although it has numerous small (~1 m) bushes spaced ~10 m apart, these do not appear to contribute to the radar return. An important aspect of this flow is the radar-bright margin which corresponds to the blocky, ~5 m high flow front. The margin is radar-bright over a wide range of viewing directions and is attributed to the blocks which act as radar reflectors. The surface of the

weathered flow has a very similar radar return to the surrounding, non-volcanic surface covered by aeolian or fluvial sediments. Thus, weathered and degraded basalt flows may be difficult to distinguish from other surfaces solely on their reflectance properties; however, the lobate bright features on the radar image which correspond to the flow margin may be an important diagnostic characteristic.

Although there is a good correlation between thickness of mantling sediments and radar brightness, this relationship cannot be extended directly to a correlation between radar brightness and flow age. In cases where the surface mantle is produced by *in situ* weathering of the flow, older flows have lower radar returns. However, some old flows have not been mantled and are radar bright, as shown in Figure 13b where the raised mountain block in the background is one of the oldest flows in the Pinacate field, yet is radar bright (Fig. 12). One explanation may be lack of an aeolian mantle due to elevation of the flow above the surrounding surface.

The characteristics of mantling materials can be determined by comparison of radar and visual images. For example, two areas within the Pinacate field appear radar-dark, suggestive of some degree of mantling (Fig. 2a *T 5* and *U-V 7*). However, one area is bright on the Skylab image (Fig. 3a *T 5*) and the other is dark (Fig. 3a *U-V 7*). The optically-bright surface may be mantled by either windblown material or by clays weathered from the basalt and ash deposits. Conversely, the dark area may be covered by pyroclastics or desert pavement composed of basalt fragments. The combination of radar and visual images is important in distinguishing between these two surfaces generated by different geological processes.

3.5. Maars and cinder cones

Three of the largest maar craters in the Pinacate region, Elegante, Colorado, and MacDougal are shown in Figure 14, each of which has a distinctive

radar return which can be related to rim morphology. Elegante (Fig. 14a,b) has the simplest rim which is raised ~70 m, forms an unbroken inner slope of ~35°, and has a symmetric exterior slope. The rim crest and inner slope appear in the SIR-A image as a symmetrical, exterior-bright collar, suggesting that this region is covered by blocky material. A distinct radar shadow occurs on the inner slope in the position expected from the incident angle geometry. The presence of this shadow indicates that the rim has a slope greater than ~40°, consistent with ground observations. The exterior rim of Elegante is rock-free, consistent with the relatively low radar return. Away from the crater rim, ejecta materials are dissected by channels, which probably accounts for the moderate radar return.

Cerro Colorado (Fig. 14c,d) also has a radar-bright inner rim slope, due to rocks and bedrock outcrops, although the width of this rough slope is much smaller than on Elegante. As with Elegante, the floor is generally dark, although there is a bright patch of material on the SE side of the floor associated with a slump feature seen from the air. One of the primary differences between Cerro Colorado and Elegante is the bright, asymmetric exterior rim slope. This asymmetry is caused by a thick deposit of ash (Donnelly, 1974) which forms a steep slope facing the radar beam. Moreover, there is a "halo" of low radar return from the proclastic deposits around Colorado. This region appears very smooth and ungullied and is a deposit of mm-sized pyroclastics.

Like Cerro Colorado and Elegante, MacDougal Crater (Fig. 14e,f) has a radar-bright inner rim slope and a dark floor, but in contrast, the rim closest to the radar viewing direction has a terraced inner wall which generates a combination of bright return and radar shadow. The exterior rim has an intermediate return similar to Elegante, as expected for its relatively coarse,

gullied surface. The area where fluvial and windblown sediments encroach, west of the rim, is radar-dark.

One circular feature which appears similar to the maar craters, but has not been identified as volcanic is shown in Figure 14g,h. Like the maar craters, it has a radar-bright rim and a dark floor. The width of the bright rim is smaller than the maar craters and there is no indication of a radar shadow, suggesting that the interior slope is less than ~40°. Despite these differences it is apparent that several geologic processes, including the formation of playas (Christensen et al., 1983), can produce structures with radar characteristics that are similar to maar craters.

3.6 Structural Features

Numerous faults and other structural features in the study area are visible on the SIR-A image. In some cases, these features are better defined on radar than on visual images. Figure 15 shows a fault block of Quaternary basalt (Donnelly, 1974) with a well-defined linear fault boundary (Fig. 2a *M 4*). Other fault-related features are visible in the surrounding mountains (Fig. 2a *M 2*).

Figure 2a (*Q 9*) shows a structural feature which is much more apparent on radar than on visual images. This feature is a raised block which has a very similar trend to other tectonically-controlled mountains in the area. Although its color and albedo are similar to the surrounding aeolian sediments (making it difficult to see on orbital photography) the differences in texture and slope in comparison to the surrounding smooth surfaces make it readily visible on radar.

4.0 Field Studies

Field studies were carried out in order to assess small-scale structures that may be important in the interpretation of SIR-A images. Eleven sites were analyzed in the eastern and western parts of the Pinacate field and the summit area, all chosen to represent the full range of radar patterns. The primary

objective was to determine size distributions of surface materials, including outcrops, and to assess the type, size, and spacing of vegetation.

For some sites, linear traverses as long as 800 m were made, with sample stations 4 m^2, spaced at 10 m intervals. At each station, percentages of six classes of material were determined: bedrock, boulders (>25 cm), cobbles (10 to 25 cm), gravels (0.2 to 10 cm), sand (0.005 to 0.2 cm), and silt-clay (~0.005 cm) fragments. At alternate stations (every 20 m), the height and spacing of vegetation were recorded in four categories: low grasses, bushes (< 2 m), trees (> 2 m) and large cacti (>2 m). Additional information pertinent to radar return, such as occurrence of ridges, washes, and local slopes, was also recorded. In addition to the traverses, several areas were assessed at larger, less regular intervals in order to note ridge heights and spacing, occurrence of bedrock outcrops, and spacing between trees.

From eleven sites studied, five were selected as representative of the surface types observed and of the contributions which rocks and vegetation make to observed radar returns. In addition, a field traverse was conducted to the summit area to correlate variations in surface texture and morphology with radar return.

4.1 Site 1

Site 1 (Fig. 16 *D 4*) is a radar-dark surface located 5 km south of MacDougal crater. On aerial photographs this is a visually bright surface. The area is generally flat and has a maximum topographic relief of 2 m which occurs in small dry washes. The distribution of rocks and vegetation was determined for a 300 m traverse (Fig. 17). No bedrock, boulders, or cobbles are exposed in this area and the largest particles are 3 to 4 cm basalt and scoria gravels which cover less than 20% of the surface area. The remaining 80 to 100% of the surface is covered with coarse sand (1-2 mm) and silt/clay (Fig. 18). Vegetation consists

of 0.5 to 1.5 m high creosote bushes spaced 2 to 4 m apart, with low grasses covering 20 to 80% of the surface and a few occasional saguaro cacti but no trees. The lack of large rocks and bedrock agrees with the low radar returns.

This site shows that the high occurrence of 3 to 4 cm particles has little effect on radar backscatter and that creosote bushes, which are somewhat larger and more closely spaced here than typically found in the region, are not good radar scatterers.

4.2 Site 2

Site 2 is located at the base of a 10 to 15 m high lava flow front and extends 400 m to the south (Fig. 16 *E* 2). Surface characteristics are summarized in Figure 19 and representative views shown in Figure 20. The surface is covered by material significantly coarser than at Site 1, with bedrock and boulders occurring along isolated ridges that are 1 m high and 20 to 30 m long. Well-developed desert pavement composed of 1 to 3 cm gravel covers the surface except along 0.5 m deep washes spaced 100-200 m apart; cobbles cover 5 to 10% of the surface. Vegetation consists of 1 m high creosote and other shrubs at spacings ranging from 5 to 40 m. Trees up to 5 m high commonly occur within the washes.

Despite increased surface roughness, this site does not have a significantly higher radar return than Site 1. There are, however, localized radar-bright points which may be associated with boulder-strewn ridges. Site 2 provides constraints on the size and abundance of rocks which can be present, but not result in substantial radar backscatter: at the radar illumination geometry of SIR-A, a level surface covered with 5-10% 10 to 15 cm cobbles appears smooth to the 23.5 cm wavelength radar beam.

4.3 Site 3

Site 3 is in a region of variable radar-bright and radar-dark returns over a weathered basalt flow surface (Fig. 16 *D 4*; Fig. 21). Because of large-scale variations in radar intensity in this area, two traverses were conducted to sample surface particle-size distributions over a large region. Maximum relief (<2 m) results primarily from small washes. Boulder and cobble abundances (Fig. 22) are higher than on the radar-dark areas at Sites 1 and 2 and this increase in surface roughness is consistent with the increase in radar brightness. Moreover, the abundance of large rocks along the two traverses agrees well with the non-uniform radar returns. Figure 23 illustrates the rock size variation, especially for 10 to 30 cm cobbles. Rock sizes are well above values for Rayleigh scattering and should produce strong radar backscatter (Beckmann and Spizzichino, 1963). The abundance and spacing of creosote and other small bushes are comparable to Site 1 and, except in washes, few large trees are present. Given the low relief, slopes have little effect on the radar reflection at this site. Thus, the primary source for radar backscatter are the 10 to 30 cm cobbles and small boulders which cover up to 40% of the surface.

4.4 Site 4

A second region of intermediate and variable radar brightness was studied west of the Sierra Blanca Mountains at the boundary between the Pinacate field and the sand sheet to the west (Fig. 16 *B 10*). As at Site 3, variable radar returns correlate with large-scale (20-50 m) variations in rock abundances (Fig. 24). In addition, this site contains a series of 3 to 5 m high lava flow fronts and ridges spaced 15 to 30 m apart, capped by boulder and cobble which cover 15 to 40% of the surface. Between the topographic highs are depressions that have surfaces free of large rocks. As at previous sites, trees are found only along the banks of several major washes. Bright radar returns are due to local relief

and rocks >10 cm which cover 40% of the surface. Rock free, flat areas produce little radar backscatter.

4.5 Site 5

The brightest radar returns in the study area are from mountains, cinder cones, and walls of maar craters. Site 5 was chosen to study the correlation between slope and radar return at Crater Grande (also called Sykes Crater, Table 2; Fig. 16 *F 3*) which has the steepest (~28°) exterior slopes of the maar craters examined and displays a wide range of radar brightnesses. A radar-dark surface southwest of the crater and a variable unit to the west were studied in detail. Results of the traverse from rim crest to the radar dark region are shown in Figure 25. Several factors contribute to the strong radar returns from a crater rim exterior: from the rim crest to a point 120 m downslope, the surface is smoothly mantled with gravel (Fig. 26a) and vegetation-free, but has a high slope (~28°). Where the slope decreases from 28° to 15° (traverse station 14) there is a rapid increase (up to 15%) in boulders and the beginning of a gullied zone (Fig. 26b) which extends to the crater perimeter. Gullies radial to the crater occur at 60 to 80 m spacing and are good radar reflectors. They are as wide as 20 m, 6 to 8 m deep, and have slopes up to 32°. Tuff beds are exposed in gully walls (Fig. 26b) and numerous basaltic boulders occur in the walls and floors.

A second break in slope (decrease from 8° to 3°) occurs at 400 m from the rim crest. The gullies terminate and boulders and outcrops of tuff beds are no longer exposed. Beyond this point, the slope flattens and the surface consists of clay/silt and gravels, with scattered patches of small cobbles. The abrupt change in surface properties observed at this point correlates with a sharp radar boundary between a strong return from the rim slope and a weak return from the flat-lying surface. Despite the wide range in slope and potential radar

reflectors, there is little variation in radar return on the rim slope. Radar returns appear to be a combination of these factors, such that increases in the surface roughness offset slope decreases and produce nearly constant radar returns.

4.6 Summit Area

The southernmost shield complex is the highest part of the Pinacate field (Fig. 4). Although radar layover has displaced the topography from plan-view locations, the radar signatures and their shapes can be identified with the ground features in the field. The summit area generally has a mottled radar reflectivity, but isolated regions on the shield also are bright or dark (Fig. 2b, *V-W 7*). A 10 km excursion crossed these areas (Fig. 27) in order to describe the surface characteristics.

The first part of the excursion crossed a subdued lava flow which produced an intermediate radar response (Fig. 27, *E 5-6*) consistent with the results presented in section 3.4. Topography was undulating, with ridges and valleys separated by 30 m to 70 m and vertical relief ranging from 5 m on the east to 10 m on the west. Basalt cobbles and boulders 20 to 50 cm in diameter covered <15% of the surface, with the remainder primarily composed of 1 to 5 cm basalt gravels (Fig. 28a). Rough bedrock outcrops occur as ridges or large blocks 3 to 5 m high, separated 50 to 75 m apart (Fig. 28b). The intermediate radar response is probably due to both the varying topography and the variable boulder and bedrock distribution.

The large, irregularly-shaped radar dark region west of the subdued lava flow (Fig. 27, *D 5-6*) has many of the characteristics of the radar-dark site 1 discussed earlier, except that fine-grained particles on the surface consist of basaltic cinders and lapilli (Fig. 29a) instead of aeolian sand and silt. Patches of bedrock and basalt boulders occur at >50m spacing but represent at

most a few percent of the surface area; cobbles also cover less than 1% of the surface. Low (m-sized) bushes dominate the vegetation but large woody trees and cacti are rare and are spaced >50 m apart (Fig. 29b). The low vegetation increases in abundance toward the summit but the radar response remains dark. The cinder cones also have dark radar signatures, even though the dominant gravel size increases to 1 to 3 cm, except where spatter/agglutinate beds are exposed on a few cinder cone summits.

A fresh aa basalt flow extends down the northeastern part of the shield (Fig. 30a). This flow has a bright radar signature (Fig. 27, *D-E 6*) and a typical clinkery surface composed of 10 to 30 cm cobbles (Fig. 30b). The eastern portions of the flow surface consist of numerous plates of frothy lava; plates are 5 to 10 cm thick and 50 to 100 cm across and project above the flow (Fig. 30c), which evidently provide numerous reflecting faces to produce a bright radar return.

4.7 Flow fronts and washes

Numerous bright linear features are visible on the radar image over the Pinacate volcanic field (Fig. 2a), several of which were investigated to determine their characteristics. All those observed were either lava flow fronts or large, tree-lined washes. Flow fronts ranged in height from 7 to 15 m and most were composed of a series of benches with slopes ranging from horizontal to vertical, but averaging 35° to 45°. The flow fronts consisted of boulders and blocks from 0.5 to 1.5 m across (Fig. 31). In most cases the flow front is radar-bright regardless of the orientation of the front relative to the radar look direction. This observation indicates that surface roughness, rather than slope, is the dominant factor in producing a strong radar reflection.

An individual flow that is distinct on the radar image (Fig. 2 *X 7-8*) was also investigated. This flow stands approximately 3 m above the surrounding

terrain and lacks a well-defined flow margin, consistent with the lack of a radar-bright return. The flow, which is covered by approximately 10-20% cobbles and boulders, is observable on radar primarily due to the low radar return from the smooth, rock-free surfaces surrounding the flow.

Several radar-bright washes were also studied. These features were 2-5 m wide and generally had abundant boulders and bedrock blocks on the floors (Fig. 32), along with large (3-5 m) trees spaced 10 to 20 m along both banks. Several radar-bright washes observed on the eastern margin of the field (Fig. 2 *W 7*) contained numerous large trees, but had very few exposed rocks on their floors. This finding indicates that trees alone are capable of producing the bright return seen in some washes. The combination of large rocks and closely-spaced trees produces strong radar returns even at a ground resolution of 50 m, indicating that the SIR-A radar was capable of detecting radar reflectors well below the spatial resolution limit.

4.8 Vegetation

These field studies indicate a general lack of radar returns from desert vegetation in the Pinacate region. Such common desert bushes as creosote (Larrea sp.) and brittlebush (Encelia sp.), did not produce significant returns, even from plants as tall as 2 m.

At one locality (Fig. 16 *F 1*), however, 3 to 4 m palo verde trees (Cerdidium sp.) and mesquite trees (Prosopis sp.) spaced 10 to 15 m apart (Fig. 33) are considered to be responsible for radar-bright returns. The site is on the floor of Badillo crater and appears as a radar-bright, visually-dark patch. The largest particles on the crater floor are gravels which occur only along the inner rim. In the heavily vegetated central region, the substrate is composed entirely of clay/silt particles.

5.0 Summary and Conclusions

The Gran Desierto-Pinacate region of northwestern Sonora, Mexico constitutes an area in which aeolian and volcanic processes dominate the surficial geology. In order to assess the appearance of features associated with these processes on orbital radar images, a study was undertaken involving image interpretation and field work. SIR-A images were compared with previously-obtained radar images and with photographs obtained from orbit, aircraft, and the ground. Field studies were conducted to measure such factors as topographic roughness, sizes and coverage of particles on the surface, and vegetation.

Results from this study show the following:

1. Sand dunes are poorly discerned on SIR-A images, evidently due to the high radar incidence angle (50°); Seasat, with an incidence angle of 20°, imaged the dunes much better. Star dunes are visible as bright spots on SIR-A images, evidently due to corner reflections from the dune "arms."
2. Fluvial washes appear radar-bright due to large boulders and woody trees (if spaced <15 to 20 m apart) on floors and along margins.
3. Radar return of lava flows varies with the degree of mantling; the greater the coverage by sediments, the lower the radar return. There is no direct correlation with the age of the lava flow.
4. In general, surfaces covered by <20%, 3 to 4 cm gravels and 5 to 10%, 10 to 15 cm cobbles appear dark (smooth) on radar, whereas 40%, 10 to 30 cm cobbles and boulders appear bright (rough).
5. The exterior slopes of maar craters are radar-bright due to a combination of slope, gullies and rock abundances.

6. Lava flow fronts generally appear radar-bright, even on mantled, radar-dark flows and where the front is oriented away from radar look direction.
7. Desert shrubs and grasses do not influence radar return; however, 3-4 m high woody trees produce radar returns.
8. The volcanic-aeolian boundary is not pronounced where aeolian cover is thinnest; the boundary becomes less distinct where the flow is mantled by sand and/or basaltic erosional material.
9. The Pinacate summit appears dark and mottled due to an extensive mantling of pyroclastic material ranging in size from 0.01 to 2 cm.

ACKNOWLEDGEMENTS

We thank Daniel Ball for his assistance in acquiring and processing the photographic products used in this report and Maureen Schmelzer for her assistance in preparing the manuscript. Sue Barnett provided support for the collection of Skylab, Seasat, and SIR-A data. We gratefully acknowledge the field assistance provided by Sue Barnett, Gene Davis, Vicki Horner, Linda Jaramillo, Jeff Moore, Maureen Schmelzer, Henry Schuver, John Scott, Eilene Theilig, and Steve Williams during excursions to the Pinacate region.

REFERENCES CITED

Arvidson, R.E. and T.A. Mutch, 1974, Sedimentary patterns in and around craters from the Pinacate volcanic field, Sonora, Mexico: some comparisons with Mars, Geol. Soc. America Bull., 85, 99-104.

Beckmann, P. and A. Spizzichino, 1963, The Scattering of Electromagnetic Waves from Rough Surfaces, Pergamon, New York, 503 p.

Blom, R.G., 1983, Pinacate volcanic field, Sonora, Mexico, in Ford, J.P., J.B. Cimino, and C. Elachi, Space Shuttle Columbia views the world with imaging radar: the SIR-A experiment, Jet Prop. Lab. Publ. 82-95, 62-63.

Blom, R. and C. Elachi, 1981, Spaceborne and airborne imaging radar observations of sand dunes, J. Geophys. Res., 86, no. B4, 3061-3073.

Born, G.H., J.A. Dunne, and D.B. Lame, 1979, Seasat mission overview, Science, 204, 1405-1406.

Breed, W.J., and C.S. Breed, 1978, Star dunes as a solitary feature in Grand Canyon, Arizona, and in a sand sea in Sonora, Mexico (abs.), NASA Tech. Memo TM-78, 455, 11-12.

Breed, C.S. and T. Grow, 1979, Morphology and distribution of dunes in sand seas observed sensing, in McKee, E.D. (ed.), Sand Seas of the World, U.S.G.S. Prof. Paper 1052, 253-302.

Brown, J.S., 1923, The Salton Sea region, California, U.S. Geol. Survey Water Supply Paper 497.

Christensen, P., R. Greeley, J. McHone, Y. Asmerom, and S. Barnett, 1983, Pinacate-Gran Desierto region, Mexico - SIR-A data analysis, Geol. Soc. America (in press).

Damon, P.E., 1970, Geochemical dating studies within the Basin and Range Province of Sonora, Ann. Rpt., Geochronological Laboratories, Univ. of Arizona, Tucson, AX1-1-AX1-5.

Damon, P.E., A. Long, and J.J. Sigalove, 1963, Arizona radiocarbon dates IV: Radiocarbon, 5, 283-301.

Donnelly, M. 1974, Geology of the Sierra del Pinacate volcanic field, northern Sonora, Mexico, and southern Arizona, U.S.A., (Ph.D. dissert.), Stanford, Calif., Stanford Univ., 722 p.

Elachi, C., W.E. Brown, J.B. Cimino, T. Dixon, D.L. Evans, J.P. Ford, R.S. Saunders, C. Breed, H. Masursky, J.F. McCauley, G. Schaber, L. Dellwig, A. England, H. McDonald, P. Martin-Kaye, and F. Sabins, 1982, Shuttle imaging radar experiment, Science, 218, 996-1003.

Ford, J.P., R.G. Blom, M.L. Bryan, M.I. Daily, T.H. Dixon, C. Elachi, and E.C. Xenos, 1980, Seasat views North America, the Caribbean, and Western Europe with imaging radar, Jet Prop. Lab Publ. 80-67, 141 p.

Ford, J.P., J.B. Cimino, and C. Elachi, 1983, Space Shuttle Columbia views the world with imaging radar: the SIR-A experiment, Jet Prop. Lab. Publ. 82-95, 179 p.

Gutmann, J.T., 1972, Eruptive history and petrology of Crater Elegante, Sonora, Mexico (Ph.D. dissert.), Stanford, Calif., Stanford Univ., 235 p.

Gutmann, J.T., 1976, Geology of Crater Elegante, Sonora, Mexico, Geol. Soc. America Bull., 87, 1718-1729.

Gutmann, J.T., 1977, Textures and genesis of phenocrysts and megacrysts in basaltic lavas from the Pinacate volcanic field, Amer. Jour. Sci., 277, 833-861.

Gutmann, J.T., 1979, Structure and eruptive cycle of cinder cones in the Pinacate volcanic field and the controls of strombolian activity, J. Geol., 87, 448-454.

Gutmann, J.T. and M.F. Sheridan, 1978, Geology of the Pinacate volcanic field, in Guidebook to the Geology of Central Arizona, Arizona Bureau of Geol. and Mineral Tech. Special Paper 2, 47-59.

Hornaday, W.T., 1908, Campfires on desert and lava, Charles Scribner Sons, New York, 366 p.

Ives, R.L., 1949, The discovery of Pinacate volcano, Sci. Monthly, 54, 230-237.

Ives, R.L., 1956, Age of Cerro Colorado crater, Pinacate, Sonora, Mexico, Am. Geophys. Union Trans., 37, 221-223.

Ives, R.L., 1959, Shell dunes on the Sonoran shore, Amer. Jour. Sci., 257, 449-457.

Ives, R.L., 1964, The Pinacate, Sonora, Mexico, Calif. Acad. Sci. Occ. Paper, 47, 1-43.

Jahns, R.H., 1959, Collapse depressions of the Pinacate lava field, Sonora, Mexico, Ariz. Geol. Soc. Digest, 2, 165-184.

Jahns, R.H. and R.G. Fielder, 1952, Collapsed volcano, Engin. and Sci., 15, no. 5, 13-16.

Kovach, R.L., C.R. Allen, and F. Press, 1962, Geophysical investigations in the Colorado delta region, J. Geophys. Res., 67, no. 7, 2845-2871.

Larson, R., H.W. Menard, and S. Smith, 1968, Gulf of California: a result of ocean-floor spreading and transform faulting, Science, 161, 781-784.

Lipman, P. and R. Christiansen, 1970, Cenozoic volcanism and tectonism in western United States and adjacent parts of the spreading ocean floor; Part 1, early and middle Tertiary, Geol. Soc. America Cord. Sec., 66th Ann. Meeting, 2(2), 112.

Lumholz, C., 1912, New Trails in Mexico, Charles Scribners Sons, New York, 411 p.

Lynch, D.J., 1981, Genesis and geochronology of alkaline volcanism in the Pinacate volcanic field, northwestern Sonora, Mexico, Ph.D. thesis, Univ. of Arizona, 248 p.

MacDougal, D.T., 1908, Across Papaguería, Am. Geographical Soc. Bull., XL, 705-725.

May, L.A., 1973, Geological reconnaissance of the Gran Desierto region, northwestern Sonora, Mexico, Arizona Acad. Sci. J., 8, 158-169.

McCauley, J.F., G.G. Schaber, C.S. Breed, M.J. Grolier, C.V. Haynes, B. Igsawi, C. Elachi, and R. Blom, 1982, Subsurface valleys and geoarcheology of the eastern Sahara revealed by shuttle radar, Science, 218, 1004-1020.

McKee, E.D., C.S. Breed, and S.G. Fryberger, 1977, Desert sand seas, in Skylab Explores the Earth, NASA SP-380.

McKee, E.D. and C.S. Breed, 1976, Sand Seas of the World, U.S. Geol. Surv. Prof. Paper 929, 81-88.

Merriam, R., 1969, Source of sand dunes of southeastern California and northwestern Sonora, Mexico, Geol. Soc. America Bull., 80, 531-534.

Merriam, R., and O.L. Bandy, 1965, Source of upper Cenozoic sediments in Colorado delta region, J. Sed. Petrol., 35, no. 4, 911-916.

Norris, R.M. and K.S. Norris, 1961, Algodones Dunes of southeastern California, Geol. Soc. America Bull., 72, 605-620.

Sabins, F.F., Jr., 1978, Remote sensing principles and interpretation, W.H. Freeman and Co., 425 pp.

Settle, M. and J.V. Taranik, 1982, Use of the space shuttle for remote sensing research: recent results and future prospects, Science, 218, 993-996.

Siegal, B.S. and A.R. Gillespie (eds.), 1980, Remote Sensing in Geology, John Wiley and Sons, Inc., 702 pp.

Smith, Roger S.U., 1982, Sand dunes in the North American deserts, in Bender, G., (ed.), Reference Handbook on the Deserts of North America, Greenwood Press, 481-524.

SSEC (Solar System Exploration Committee), 1983, Planetary Exploration through the year 2000: Executive summary, NASA Report, NASA Advisory Council, 29 p.

Wilson, E.D., 1933, Geology and mineral deposits of southern Yuma County, Arizona, Univ. Ariz. Bull., 4, no. 2, 1-236.

Wood, C.A., 1974, Reconnaissance geophysics and geology of the Pinacate craters, Sonora, Mexico, Bull. Volcanol., 38, 149-172.

FIGURE CAPTIONS

Figure 1. Map of southwestern United States and northwestern Mexico showing the Gran Desierto and Pinacate volcanic field. Outlines of the SIR-A radar image, the geological map (Fig. 2), and Skylab coverage (Fig. 3) are also shown.

Figure 2a. Shuttle Imaging Radar (SIR-A) view of study area. Image was acquired on November 13, 1981 on Data Take 24C, and covering an area 50 by 120 km. Letters and numbers provide locations given in the text.

Figure 2b. Geologic map of the study area (after Donnelly, 1974) with additional interpretation based on SIR-A and Skylab images; map corresponds to area shown in Figure 2a. Numbers refer to maar craters listed in Table 2; dashed lines delineate the three main shields of Pinacate; stars and dot patterns mark prominent sand dunes. Dashed-dot lines with arrows indicate radar-bright washes. Volcanic rock units are designated Op for Pinacate shield extrusives, Ob for Pliocene-Pleistocene continental basalts, T-Ob for Cenozoic basalts and andesites and Tvr for Tertiary rhyolites, dacites, and andesites. P-Tc indicates undifferentiated crystalline rocks. Sedimentary rocks are subdivided into Os for alluvial and aeolian gravels, sands, and silt, and Opl for playa deposits.

Figure 3. Skylab images covered by SIR-A radar (Fig. 2). Figure 3a has been enhanced to reveal detail in Pinacate lava field; Figure 3b is optimized for details of aeolian surfaces.

Figure 4. Oblique aerial photograph of Pinacate lava field showing summit region and typical flows and cinder cones; view is to the north (photograph ASU 2338-A by D. Ball, Feb. 1983).

Figure 5. Oblique aerial photograph of Grande crater, one of 10 maarlike craters in the Pinacate volcano field (Fig. 2 *S 5*). View is to the northwest (photograph ASU 245-A by Ronald Greeley, 1975).

Figure 6. Gran Desierto star dunes and El Rosario Mountains (a); a) Skylab, b) Seasat, c) SIR-A. Dune forms are visible on Skylab and Seasat but are less apparent on SIR-A. Bright points on SIR-A may be due to star dune arms acting as corner reflectors.

Figure 7. Oblique aerial photographs of complex star dunes in Gran Desierto; a) view to southwest (photograph ASU 2334-A by D. Ball, Feb. 1983), b) low-altitude view of complex star dunes (photograph ASU 2333-A by D. Ball, Feb. 1983), c) individual star dune showing details of crest and arms. The star dunes are in linear rows oriented N 60°W and are separated by flat, interdune zones of compound transverse dunes; arm crests are sharply defined and vegetation-free (photograph ASU 2335-A by D. Ball, Feb. 1983).

Figure 8. Oblique aerial photograph showing the lava flow and sand interface at the southern edge of Pinacate lava field; compound barchanoid dunes are superposed with compound transverse dunes (Figs. 2 *T-X 9* and 3 *T-X 9*). View is to the east; cinder cones in center are radar bright points at *U10* Figure 2a. Dark, sinuous washes are also radar-bright in Figure 2a (photograph ASU 2339-A by D. Ball, Feb. 1983).

Figure 9. SIR-A images of major drainage networks; a) washes draining the southern edge of Pinacate field (Fig. 2a *U 9*), b) washes located at *X 5* in Figure 2a. Washes appear as radar-bright linear features due to presence of large rocks and trees.

Figure 10. Oblique aerial photographs of drainage networks in the region shown in Figure 9b. a) View showing increase in vegetation in washes

(photograph ASU 2350-A by D. Ball, Feb. 1983). b) Close-up of individual wash; vegetation is larger and denser along the sides of the wash (photograph ASU 2347-A by D. Ball, Feb., 1983).

Figure 11. Oblique aerial photographs of the volcanic field and sand border. a) View southward across the radar-sharp boundary shown at *V 9* in Figure 2a (photograph ASU 2340-A by D. BAll, Feb. 1983). b) View northward across the boundary shown *U 9* in Figure 2a; radar boundary does not correspond to visual boundary due to mantling by dark material removed from volcanic terrain (photograph ASU 2327-D by D. Ball, Feb. 1983). c) View northward across the indistinct radar boundary at *K 9* in Figure 2a; bright aeolian and dark volcanic materials interfinger to form radar diffuse boundary (photograph ASU 2343-A by D. Ball, Feb., 1983).

Figure 12. Enlargement of SIR-A image of lava flows on eastern margin of Pinacate field showing range of radar return for different flows due to differences in surface roughness and degree of mantling. Individual flows shown in Figure 13 are indicated by the corresponding letters; arrows indicate viewing direction.

Figure 13. Aerial photographs of radar-distinct lava flows. a) View southward across fresh, radar-bright aa flow (photograph ASU 2351-A by D. Ball, Feb. 1983). b) View northward of flow of intermediate radar return (foreground) and degraded, radar-bright flow (background) (photograph ASU 2329-D by D. Ball, Feb. 1983). c) Radar-dark flow with bright flow margin that is heavily mantled by aeolian and fluvial(?) materials. View is to south (photograph ASU 2354-A by D. Ball, Feb., 1983).

Figure 14. Comparisons of radar and visual images of circular features. Radar illumination is from right in all cases. a) Radar image of Crater

Elegante (#8 in Fig. 2b); b) View southeast across Elegante; radar-dark shadow is produced by steep inner wall slopes (photograph ASU 2353-A by D. Ball, Feb. 1983). c) Radar image of Cerro Colorado (crater #7 in Fig. 2b); d) View southwest of Cerro Colorado; radar-dark annulus surrounding crater corresponds to smooth tephra deposits (photograph ASU 242-A by R. Greeley, 1975). e) Radar image of MacDougal Crater (#1 on Fig. 2b) f) View southeast across MacDougal Crater showing terraced wall which produces a double bright ring with shadow zone in the radar image (e) (photograph ASU 247-A by R. Greeley, 1975). g) Radar image of playa. h) aerial photograph of playa viewed toward the east; trees around edge of playa produce radar-bright return in (g) (photograph ASU 2352-A by D. Ball, Feb. 1983).

Figure 15. View northwest of fault-uplifted block of Quaternary basalt (Figs. 2 and 3 *M 4*). Straight boundary on the right of the block is probably fault-controlled. Surface of block is radar-bright (rough), despite its older age than the basalts on the Pinacate shield (photograph ASU 2350-A by D. Ball, Feb. 1983).

Figure 16. Enlargement of SIR-A radar image of region shown between *Q-S 5-9* in Figures 2 and 3, showing field sites 1-5.

Figure 17. Surface traverse results, Site 1; the percentage of the surface covered by each component is indicated, along with the spacing of shrubs (<2 m high) and trees (>2 m high); stations were 10 m apart. This site had no surface materials larger than gravels, which is consistent with the low radar return seen in Figure 16.

Figure 18. Photograph of surface at Site 2, showing the lack of particles larger than ~5 cm (photograph ASU 2361-D by P. Christensen, April, 1983).

Figure 19. Surface traverse results, Site 2. Although bedrock outcrops, boulders, and cobbles are present, their occurrence is too low to produce a radar-bright return.

Figure 20. Site 2. a) View northwest showing traverse surface and radar-bright lava flow front in background (photograph ASU 2362-D by P. Christensen, April, 1983). b) Vertical view at traverse station 5 (photograph ASU 2362-D by P. Christensen, April, 1983).

Figure 21. Site 3. a) Oblique aerial view westward with Site 3 indicated by arrow (photograph ASU 2328-D by J. McHone, Feb. 1983). b) View westward from traverse station 1 showing dissected cinder cone seen in (a) and large rocks on surface (photograph ASU 2361-D by P. Christensen, April, 1983).

Figure 22. Surface traverse results, Site 3. a) Traverse A. b) Traverse B.

Figure 23. Variation in particle size distribution observed at Site 3; all photographs are vertical views to the same scale; a) Traverse A, Station 21 showing well-developed desert pavement (photograph ASU 2361-D by P. Christensen, April, 1983). b) Traverse A. Station 1 (photograph ASU 2361-D by P. Christensen, April, 1983). c) Traverse A. Station 10 (photograph ASU 2361-D by P. Christensen, April, 1983). d) Traverse B. Station 13. Card is 8 by 13 cm (photograph ASU 2364-D by J. Zimbelman, April, 1983).

Figure 24. Surface traverse results; Site 4 showing greater abundance of cobbles and boulders than in Sites 1, 2, and 3.

Figure 25. Surface traverse results, Site 5, and a topographic profile showing changes in the distribution of surface materials.

Figure 26. Site 5. a) Surface at traverse station 3 near rim crest (photograph ASU 2363-D by P. Christensen, April, 1983). b) View along traverse

from Station 30 showing tuff beds and boulders exposed in gullies (photograph ASU 2363-D by P. Christensen, April, 1983).

Figure 27. Part of SIR-A radar image showing the summit area of the Pinacate field. The irregular dark (radar smooth) area (*D 5-6*) extends from the summit cinder cones down the northern portion of the volcano.

Figure 28. Surface of degraded lava flow with mottled radar brightness (Fig. 27 *E 5-6*). a) Blocks and low vegetation typical of much of the surface. White card is 15 cm long (photograph ASU 2533-D by J. Zimbelman, Dec. 1983). b) Lava ridge projecting 5 m above the surface (photograph ASU 2533-D by J. Zimbelman, Dec. 1983).

Figure 29. Radar dark surface in summit area (Fig. 27 *D 5-6*). A) Vertical view of cm-sized gravel particles. Card is 15 cm long (photograph ASU 2533-D by J. Zimbelman, Dec. 1983). b) Abundant low (m-sized) bushes and widely scattered larger cacti. The nearest cinder cone is radar-dark (photograph ASU 2533-D by J. Zimbelman, Dec. 1983).

Figure 30. Relatively fresh basalt lava flow on the northeastern flank of Pinacate summit area (Fig. 27 *F 6*). A) View toward the summit of Pinacate (photograph ASU 2532-D by J. Zimbelman, Dec. 1983). b) Rounded aa clinkers on flow surface. Card is 15 cm long (photograph ASU 2534-D by J. Zimbelman, Dec. 1983). c) Lava plates projecting above the flow surface (photograph ASU 2534-D by J. Zimbelman, Dec. 1983).

Figure 31. Flows showing large rocks exposed on flow front. a) Radar-bright front located at *E 2* in Figure 16 (photograph ASU 2362-D by P. Christensen, April, 1983). b) Radar-bright front located at *F 3* in Figure 16 (photograph ASU 2365-D by J. Zimbelman, April, 1983). c) Indistinct front located at *E 2* in Figure 16 (photograph ASU 2362-D by P. Christensen, April, 1983).

Figure 32. Radar-bright washes. Both trees and large rocks are common in washes and play an important role in producing radar-bright returns (photographs ASU 2361-D by P. Christensen, April, 1983).

Figure 33. Floor of Badillo Crater (crater #4 on Fig. 2b). a) View from southern rim looking north. Vegetation consists of low (~1/2 m) shrubs except in center of crater shown at right edge (photograph ASU 2363-D by P. Christensen, April, 1983). b) Crater center showing vegetation which consists of 3-4 m high palo verde and mesquite trees spaced 10-15 m apart. These trees are responsible for bright radar return from crater seen at *E 1* in Figure 16 (photograph ASU 2363-D by P. Christensen, April, 1983).

Table 1. Images and maps used in study of Gran Desierto, Pinacate region.

Image	Designation	Area covered
Radar Data		LAT LONG
Seasat	1140	32° 10' N 115° 8' W 31° 55' N 114° 8' W 31° 20' N 114° 50' W 31° 31' N 113° 46' W
SIR-A	DT 24C	32° 46' N 114° 46' W 31° 41' N 112° 12' W 32° 14' N 115° 1' W 31° 8' N 112° 28' W
Orbital Photography		
Skylab	SL 3 86006	31° 32' N 113° 25' W 32° 7' N 112° 52' W 32° 4' N 113° 28' W 33° 14' N 112° 54' W
	SL 4 92359	31° 32' N 113° 41' W 31° 56' N 113° 1' W 32° 2' N 114° 15' W 31° 27' N 113° 35' W
Aerial Photography*		
	Zona 69 R1566-25F3	32° 09' N 113° 58' W 31° 59' N 113° 40' W 31° 52' N 114° 52' W 31° 44' N 113° 50' W
	Zona 69 R1566-27F3	32° 08' N 113° 46' W 31° 55' N 113° 27' W 31° 47' N 113° 54' W 31° 38' N 113° 35' W
	Zona 69 R1566-29F3	31° 57' N 113° 32' W 31° 50' N 113° 15' W 31° 41' N 113° 40' W 31° 34' N 113° 21' W

*Supplied by: Direccion General de Estadios del Territoris Nacional
Agencia DETENAL
Av. de los Pioneros y Andador Cholula No. 2
Centro Civico Comercial Mexicali
Mexicali B.C.N., Mexico

Table 2. Geographic names of maar and maar-like craters in the Pinacate volcano field. Crater numbers refer to Figure 3. Names used by Donnelly are adopted here.

CRATER NUMBER	Donnelly 1974, p.2	Arvidson and Mutch 1974	Gutmann 1979, p 449	DETENAL 1:50,000 Topographic Maps 1974-1980	1:250,000 JOG* 1976
1	MacDougal Crater	MacDougal	MacDougal Crater	Volcan el Verdugo	------
2	Molina Crater	-------	------	Volcan el Trebol	------
3	Crater Grande	Sykes	Crater Grande	Volcan Romo (Tinaja de los Papagos)	------
4	Badillo Crater	-------	Badillo Crater	Volcan la Tinajita	------
5	Kino Crater	------	Kino Crater	------	------
6	Celeya Grande	------	Celaya Crater	Volcan los Vidrios	------
7	Cerro Colorado	Cerro Colorado	Cerro Colorado	Cerro Colorado	------
8	Crater Elegante	Elegante	Crater Elegante	Volcan el Elegante	Cerro Colorado (error)
9	Moon Crater	------	------	Volcan la Luna	------
10	Tuff Ring	------	------	------	------

* Joint Operations Graphic

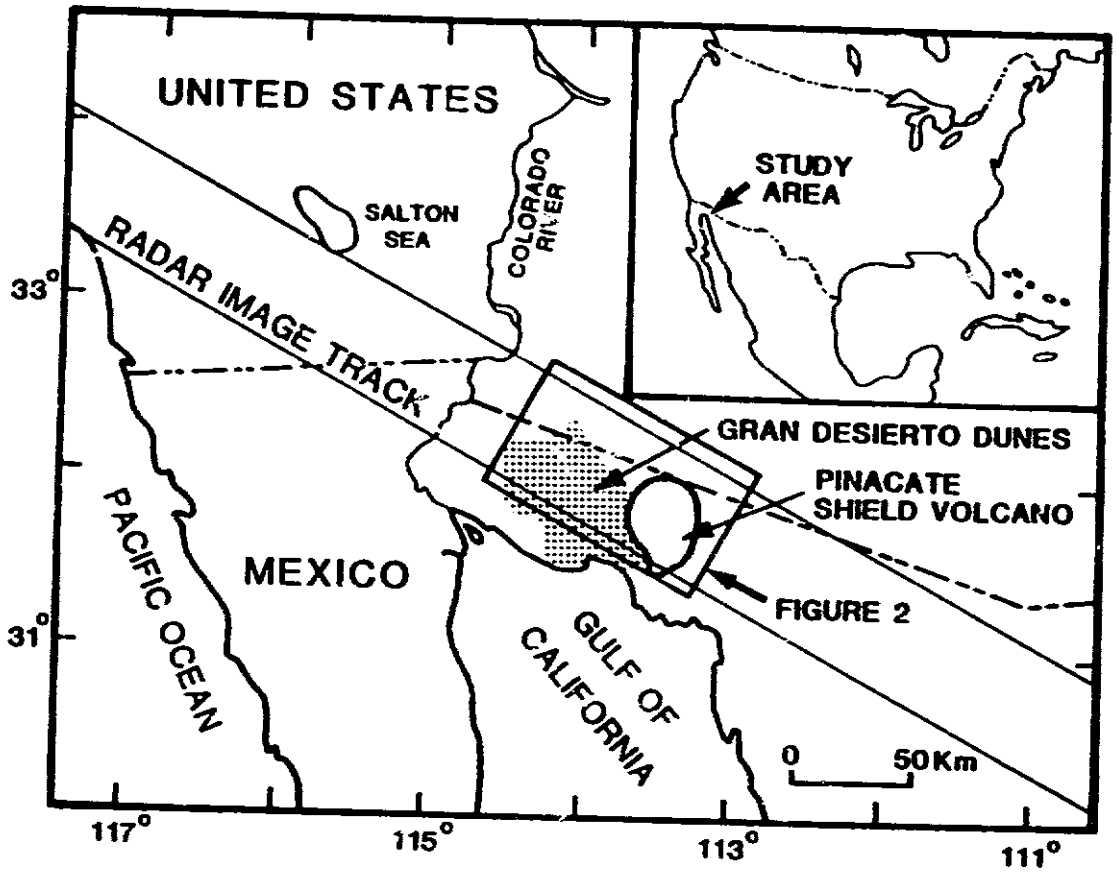
UNITED STATES
SALTON SEA
COLORADO RIVER
STUDY AREA
RADAR IMAGE TRACK
GRAN DESIERTO DUNES
PINACATE SHIELD VOLCANO
FIGURE 2
MEXICO
PACIFIC OCEAN
GULF OF CALIFORNIA
0 50Km
33°
31°
117°
115°
113°
111°

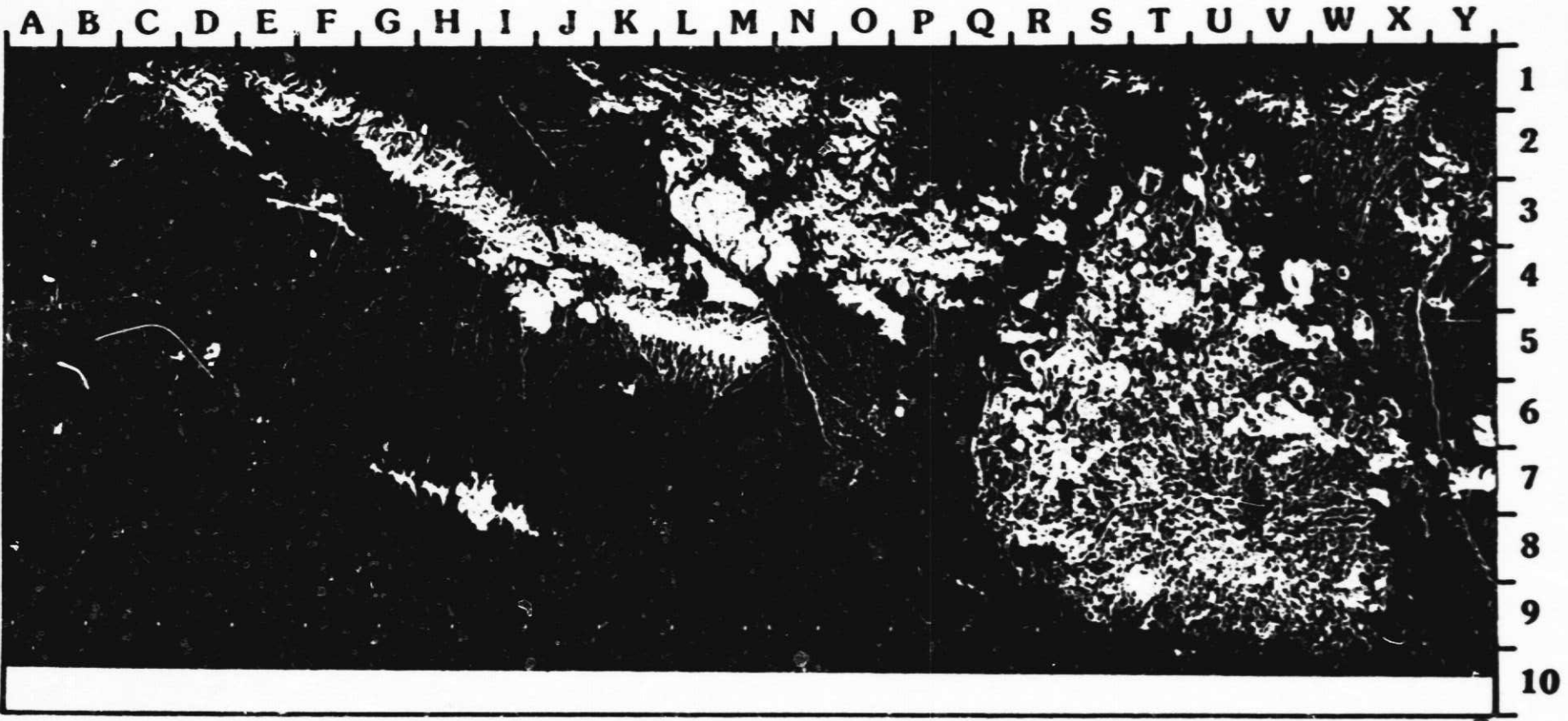

Greeley et al. Fig. 2a

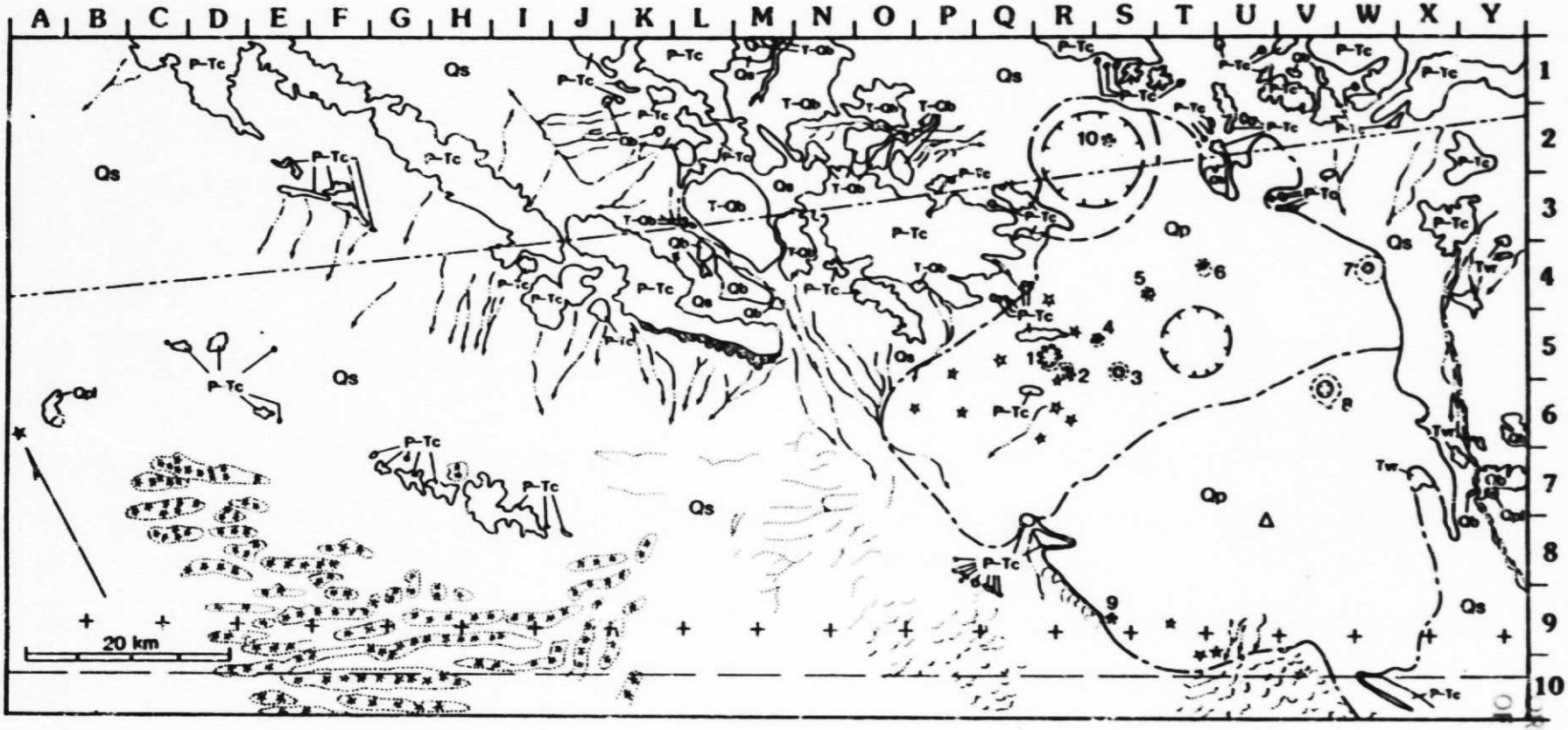

Greeley et al. Fig 2b

Greeley et al. Fig. 3a

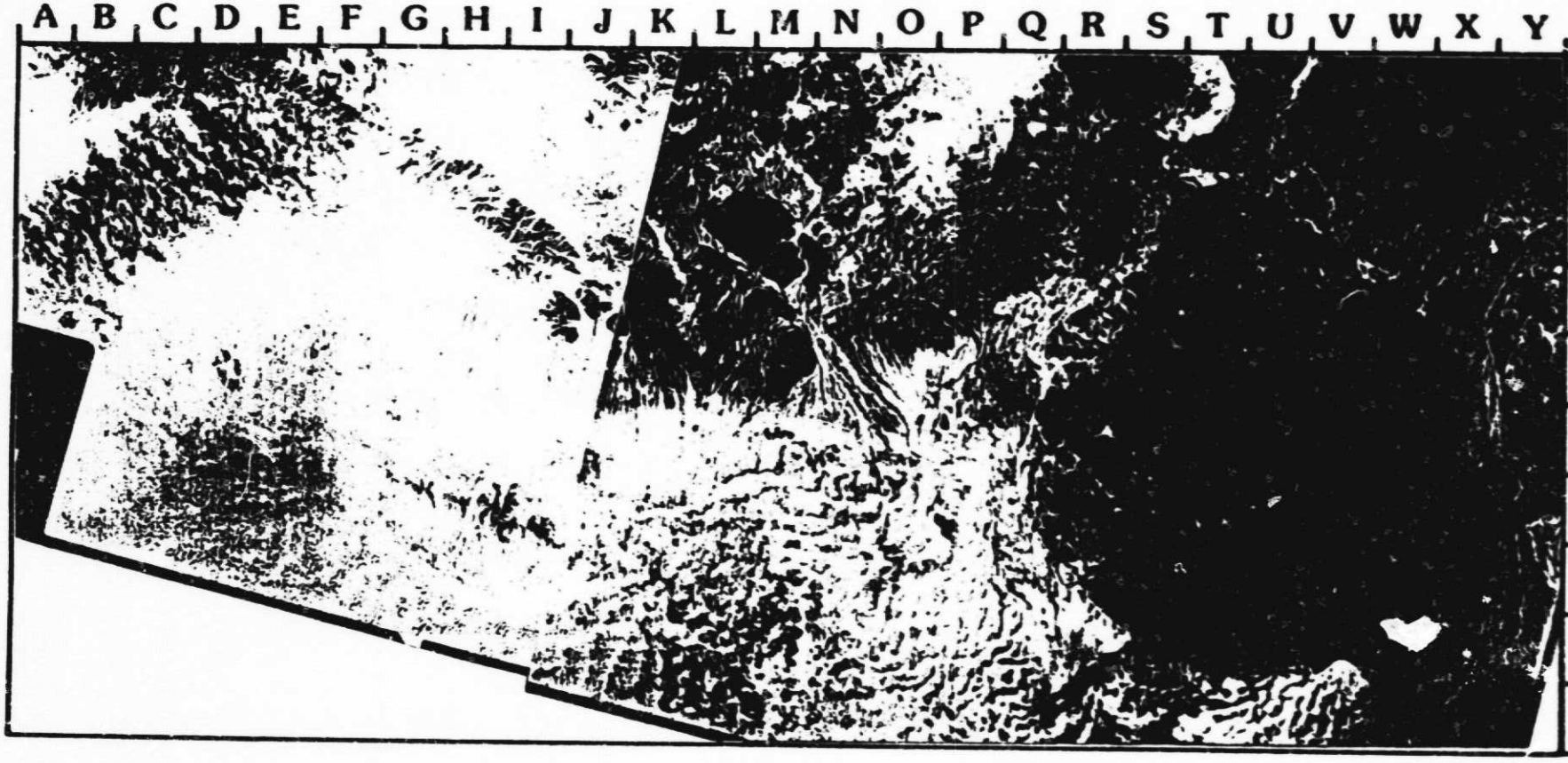

Greeley et al. Fig. 3b

Top

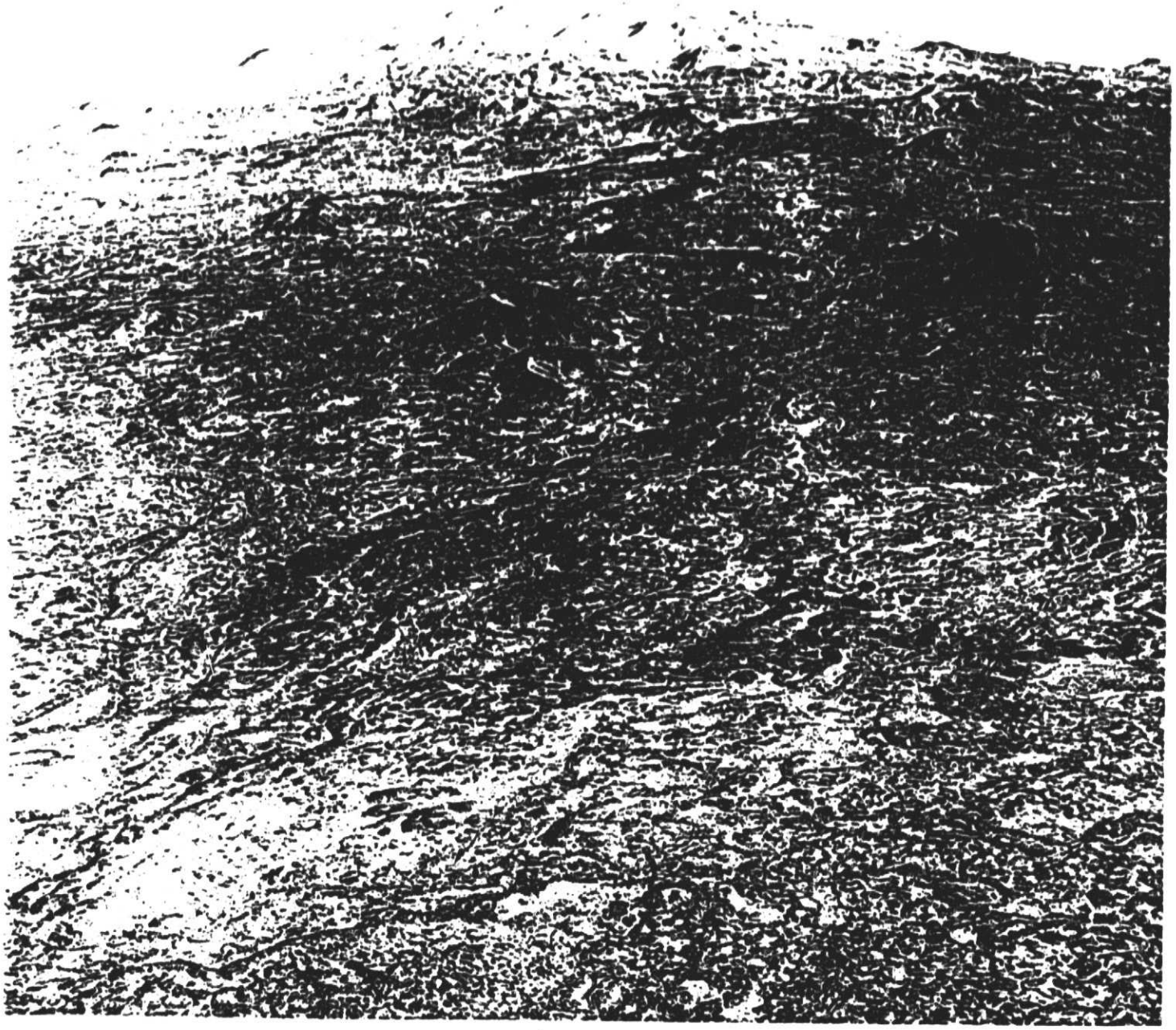

Greeley et al. Fig. 4

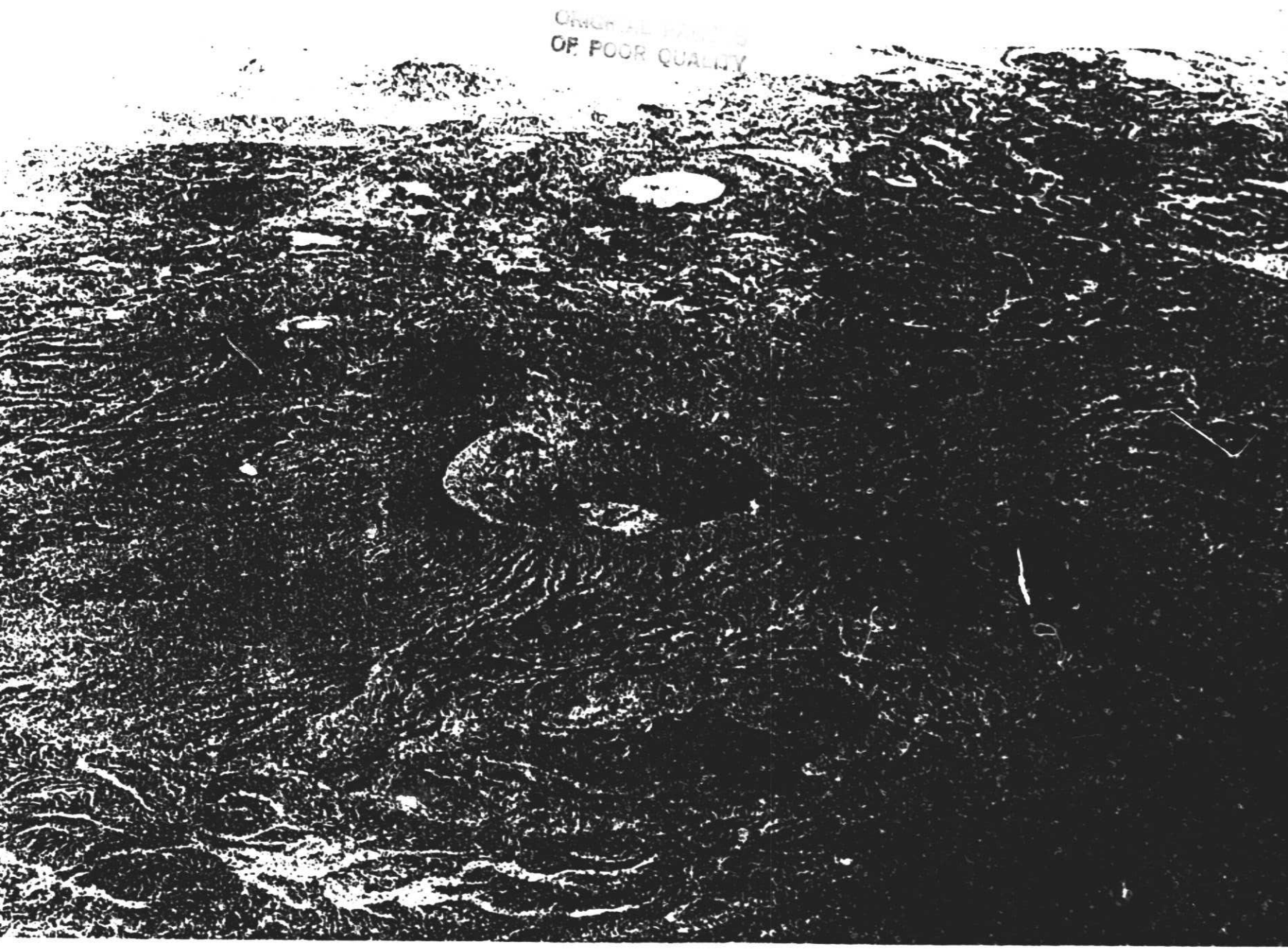

Greeley et al. Fig. 5

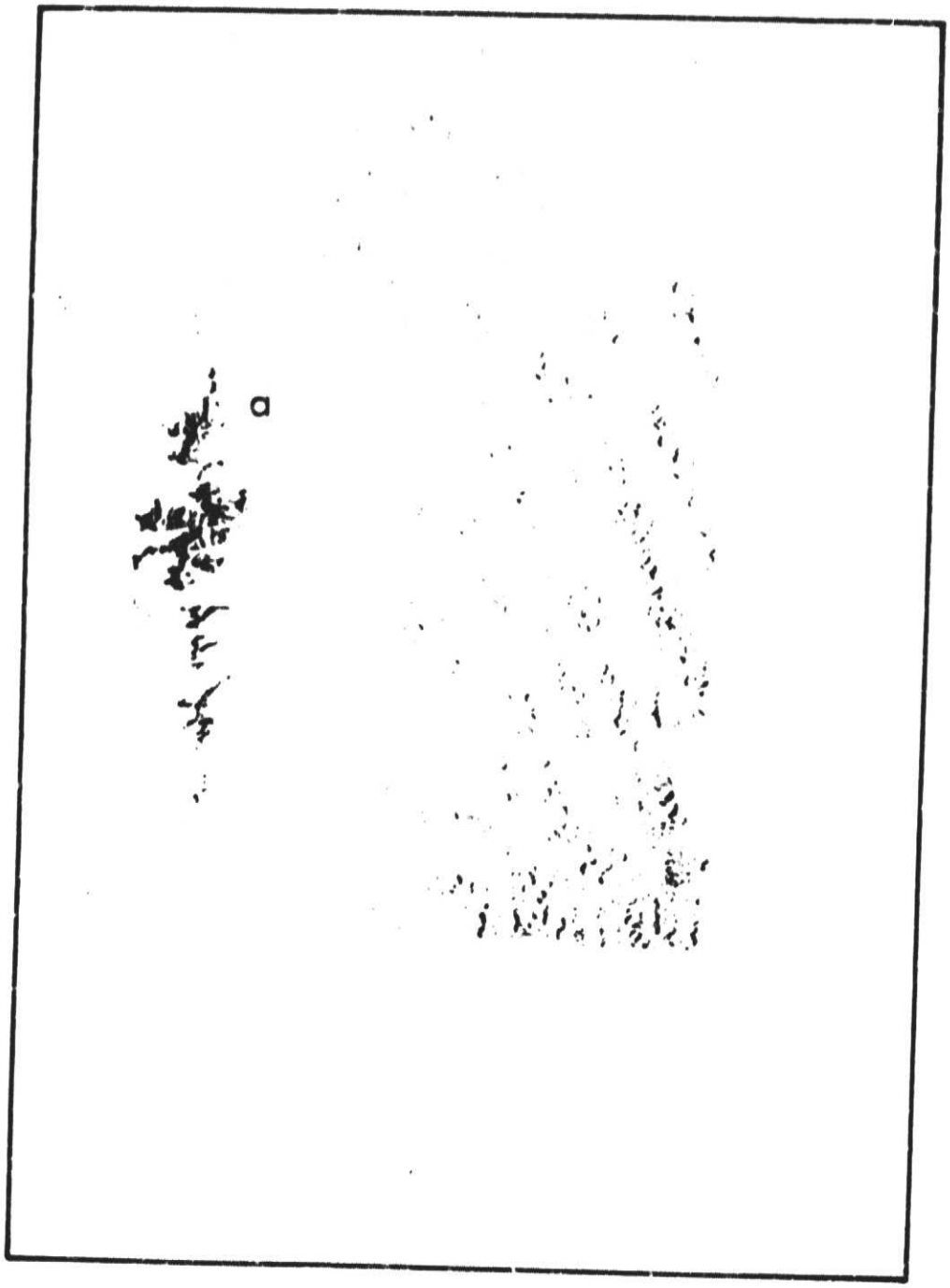

Greeley et al. Fig. 6a

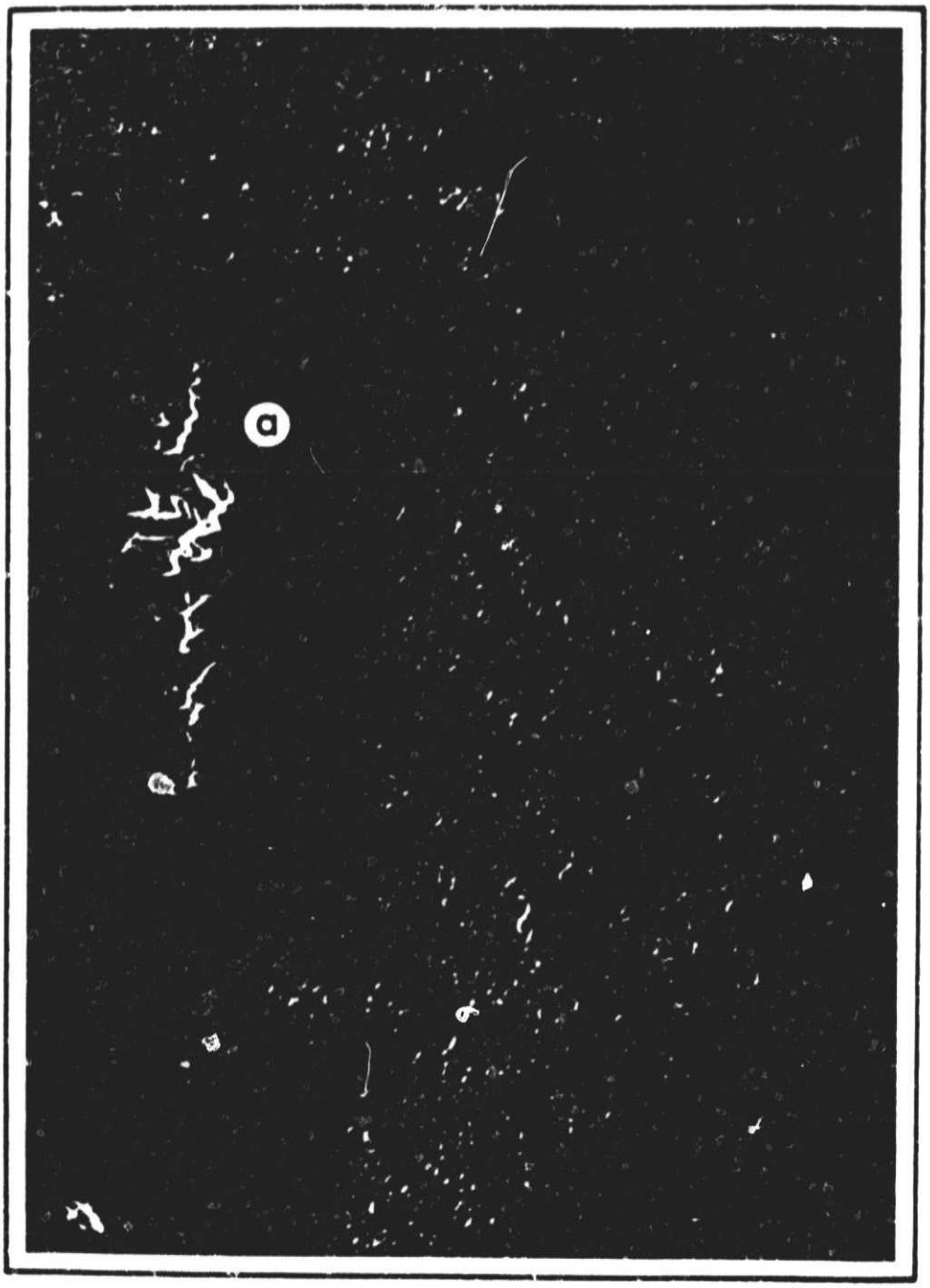

Greeley et al. Fig. 6 b

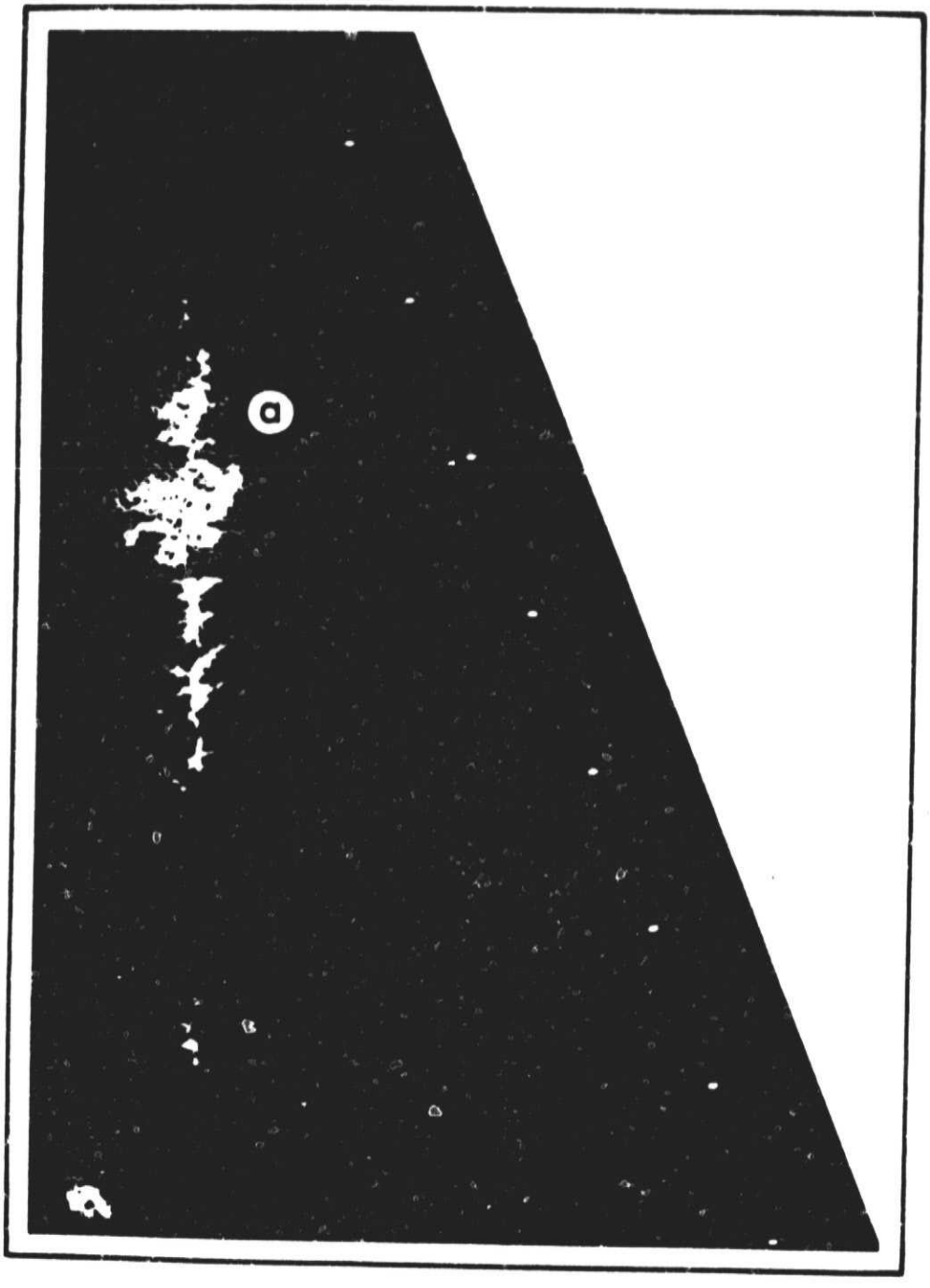

Greeley et al Fig. 6C

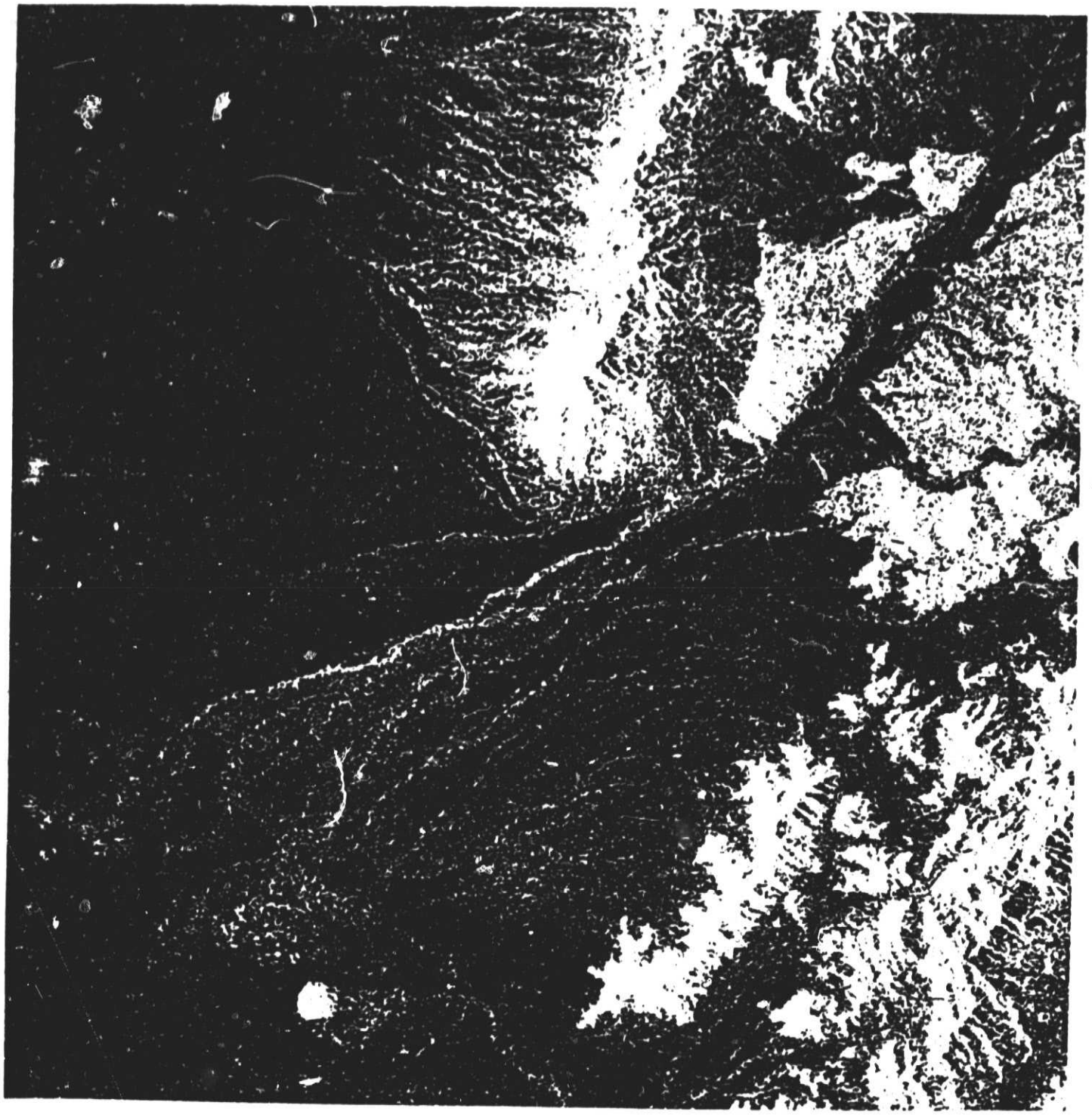

Top

Top

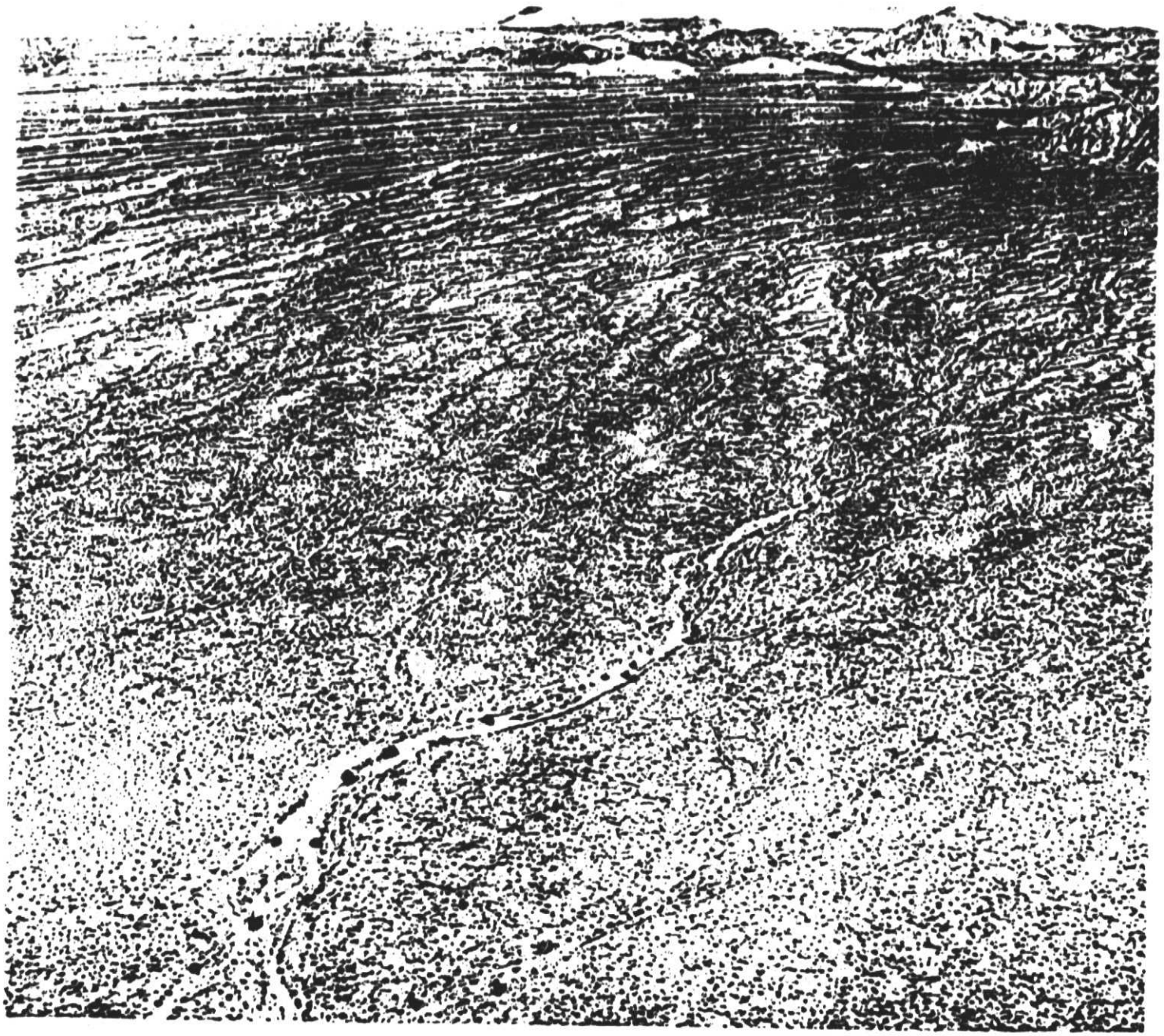

Greeley et al. Fig 10a

Top

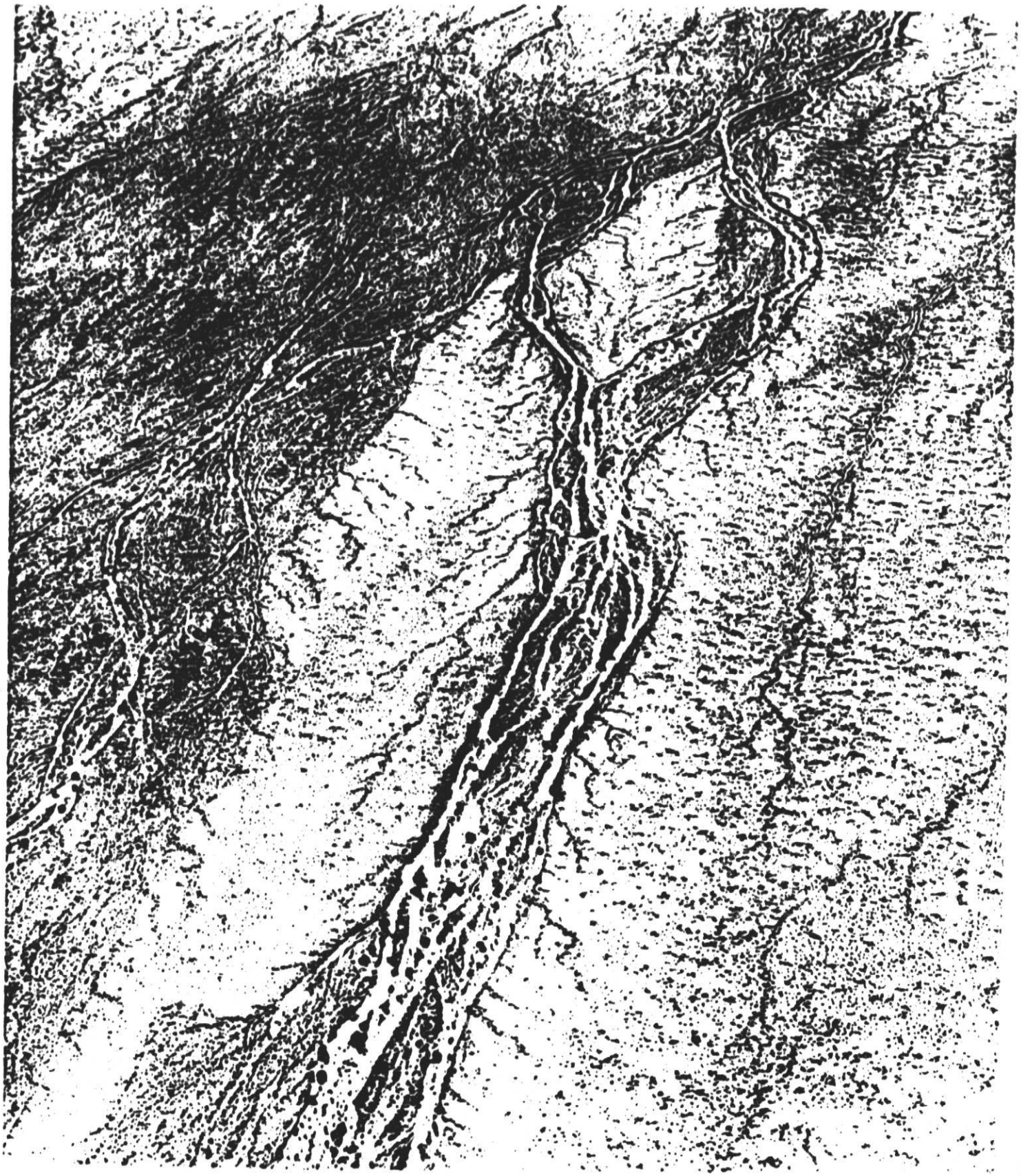

Greeley et al. Fig 10b

Greeley et al. Fig 11 a

Top

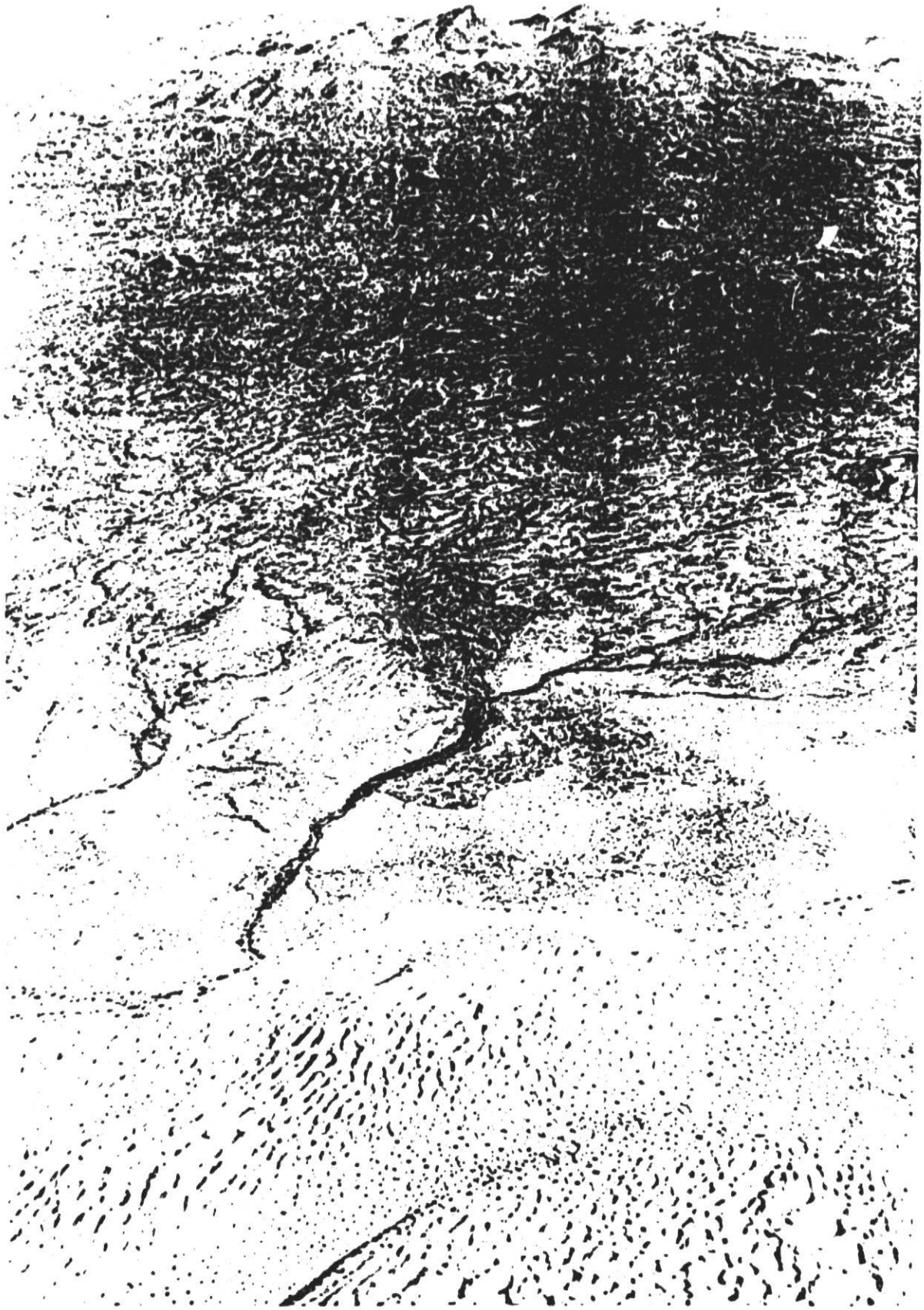

Greeley et al. Fig. 11b

Greeley et al. Fig. 11c

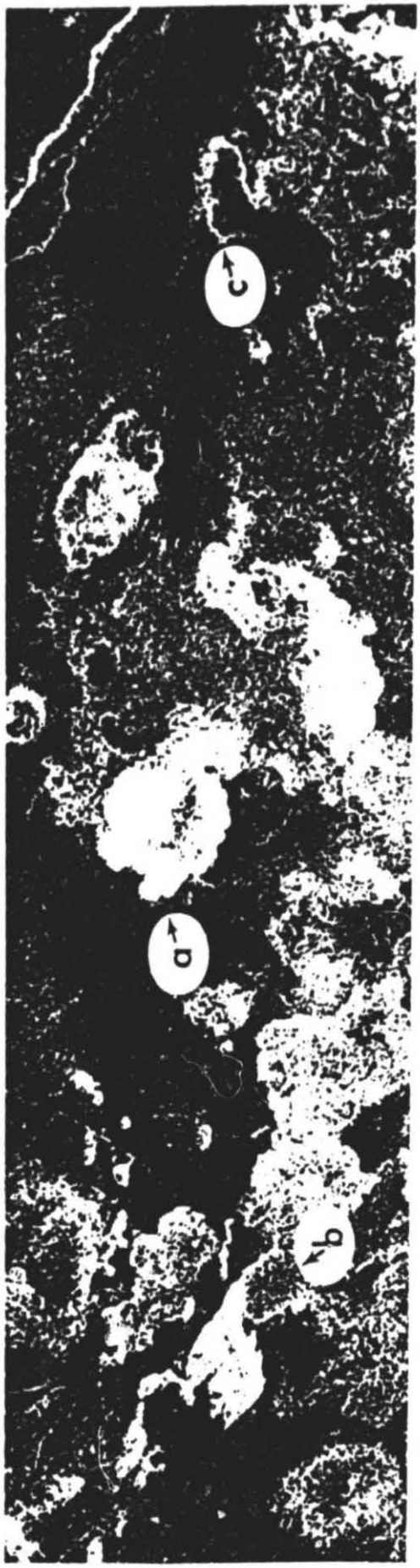

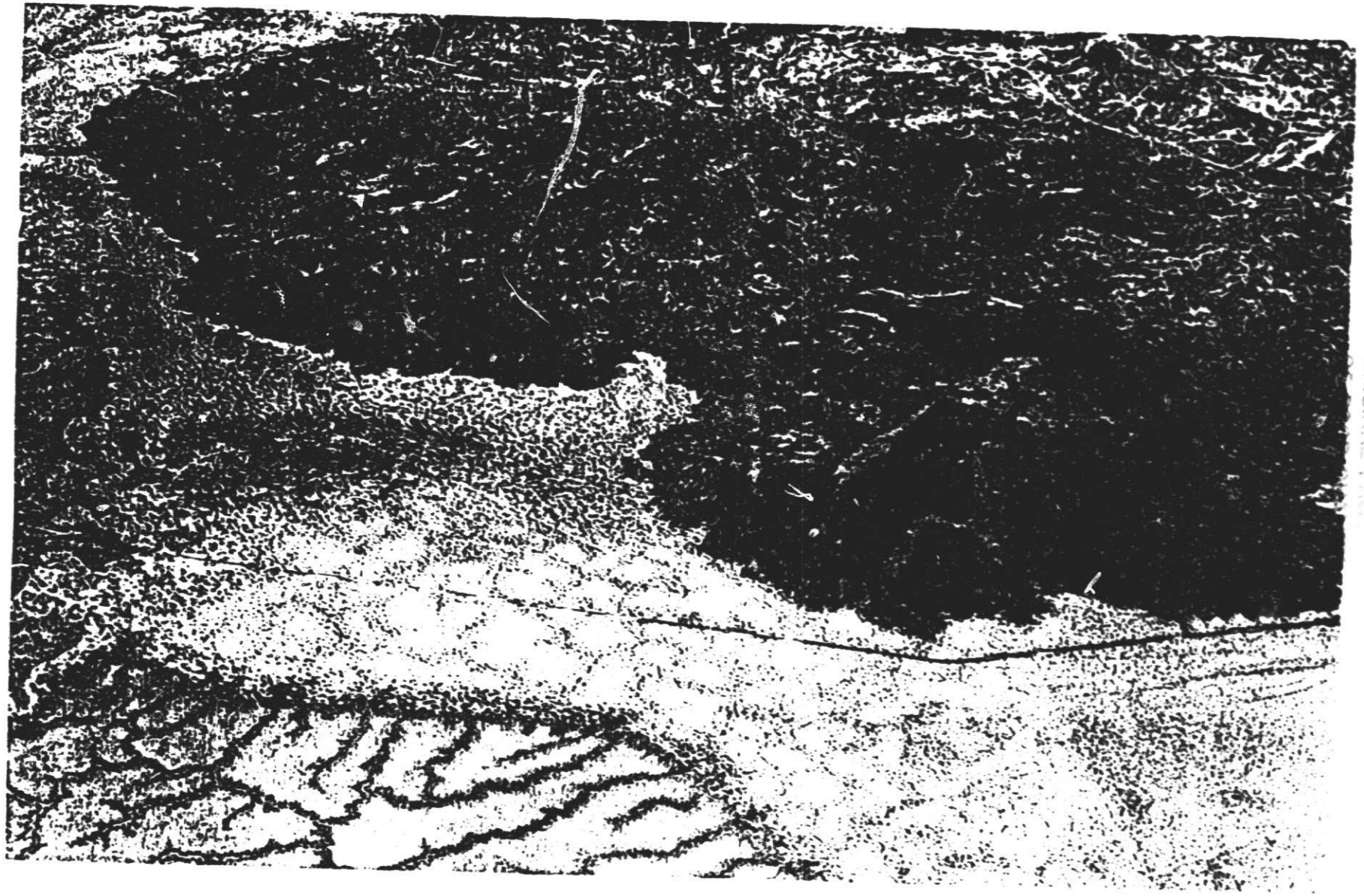

Greeley et al. Fig. 13a

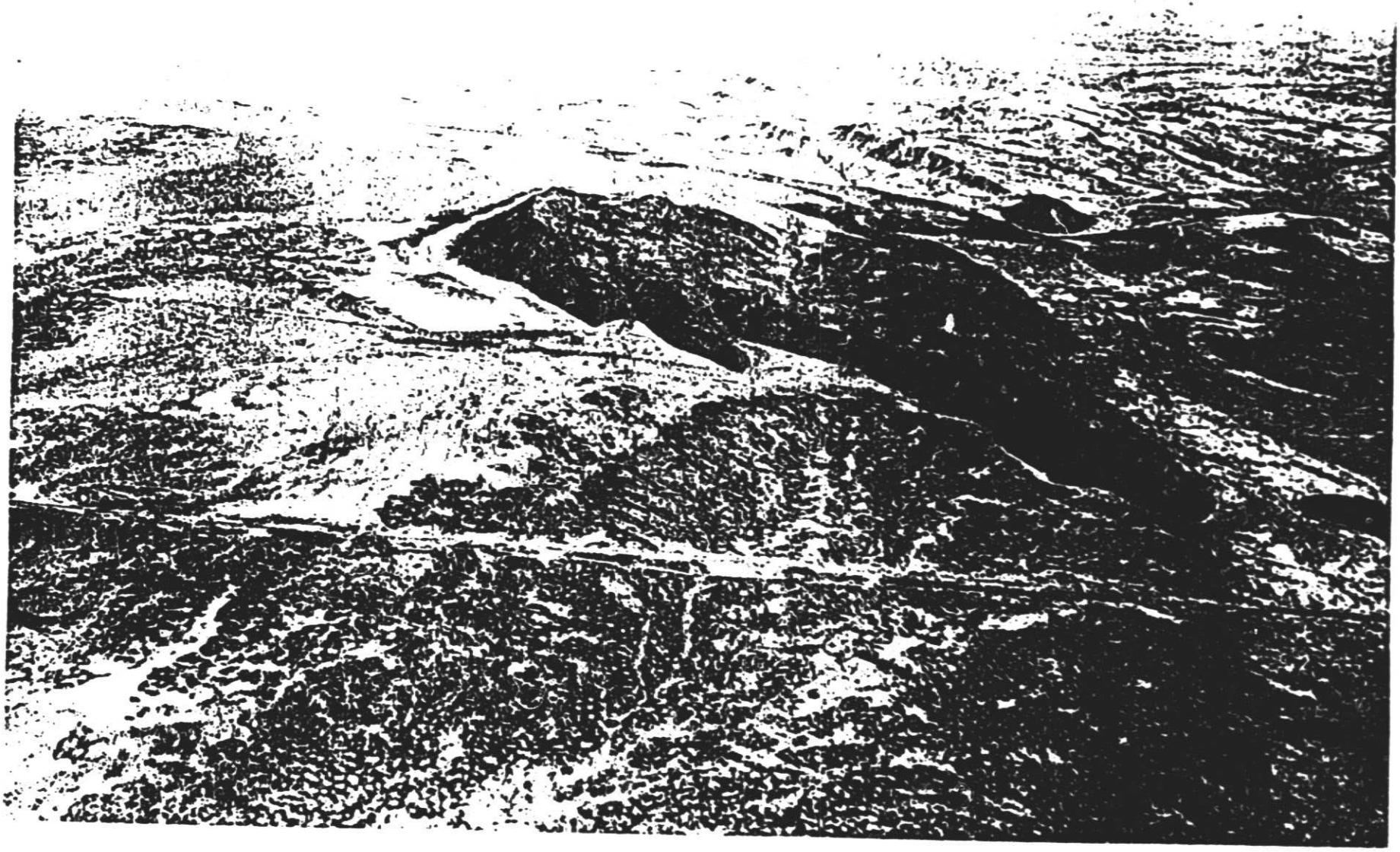

Greeley et al. Fig. 13 b

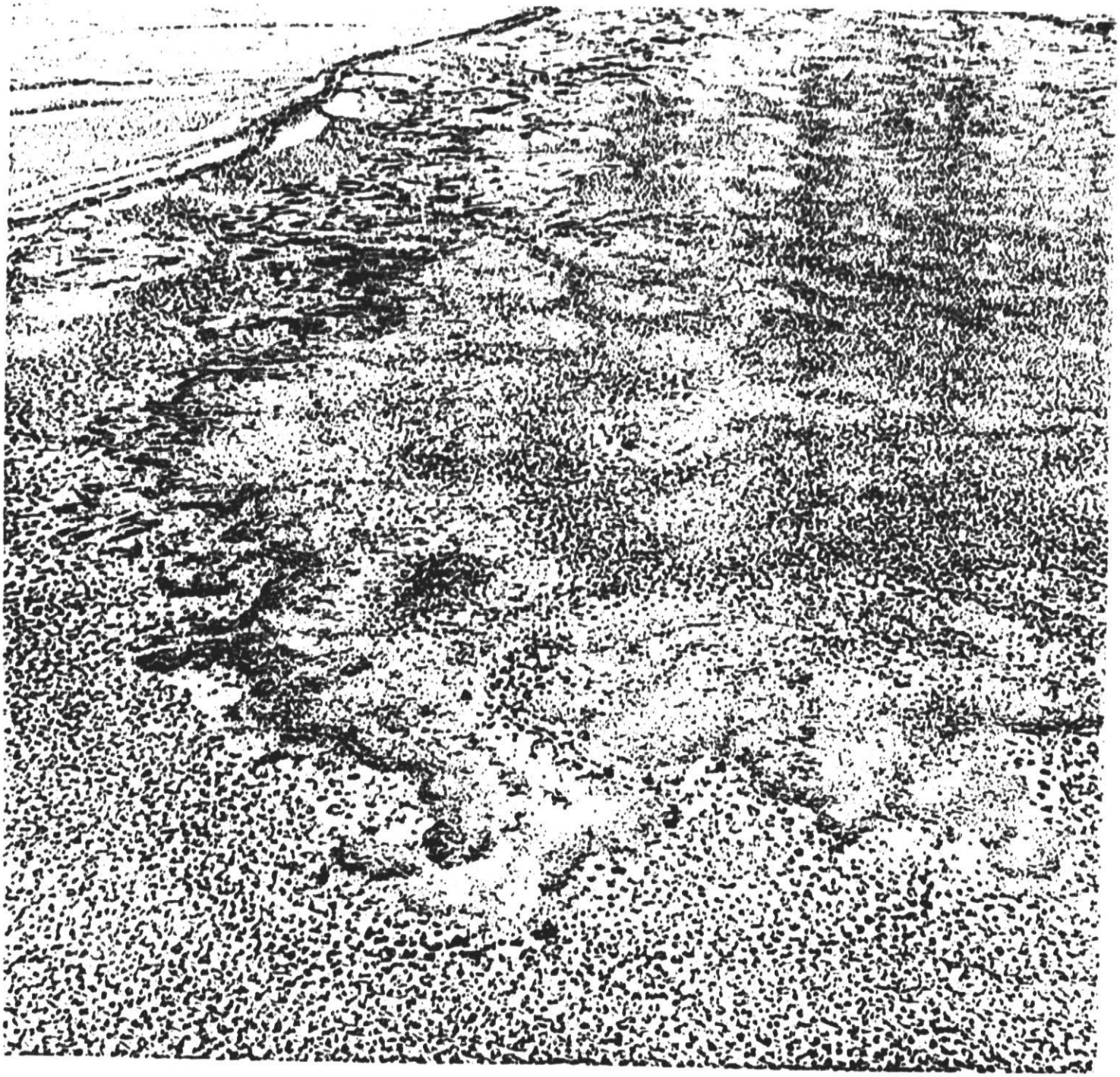

Greeley et al. Fig. 13c

Top

Greeley et al. Fig 14a

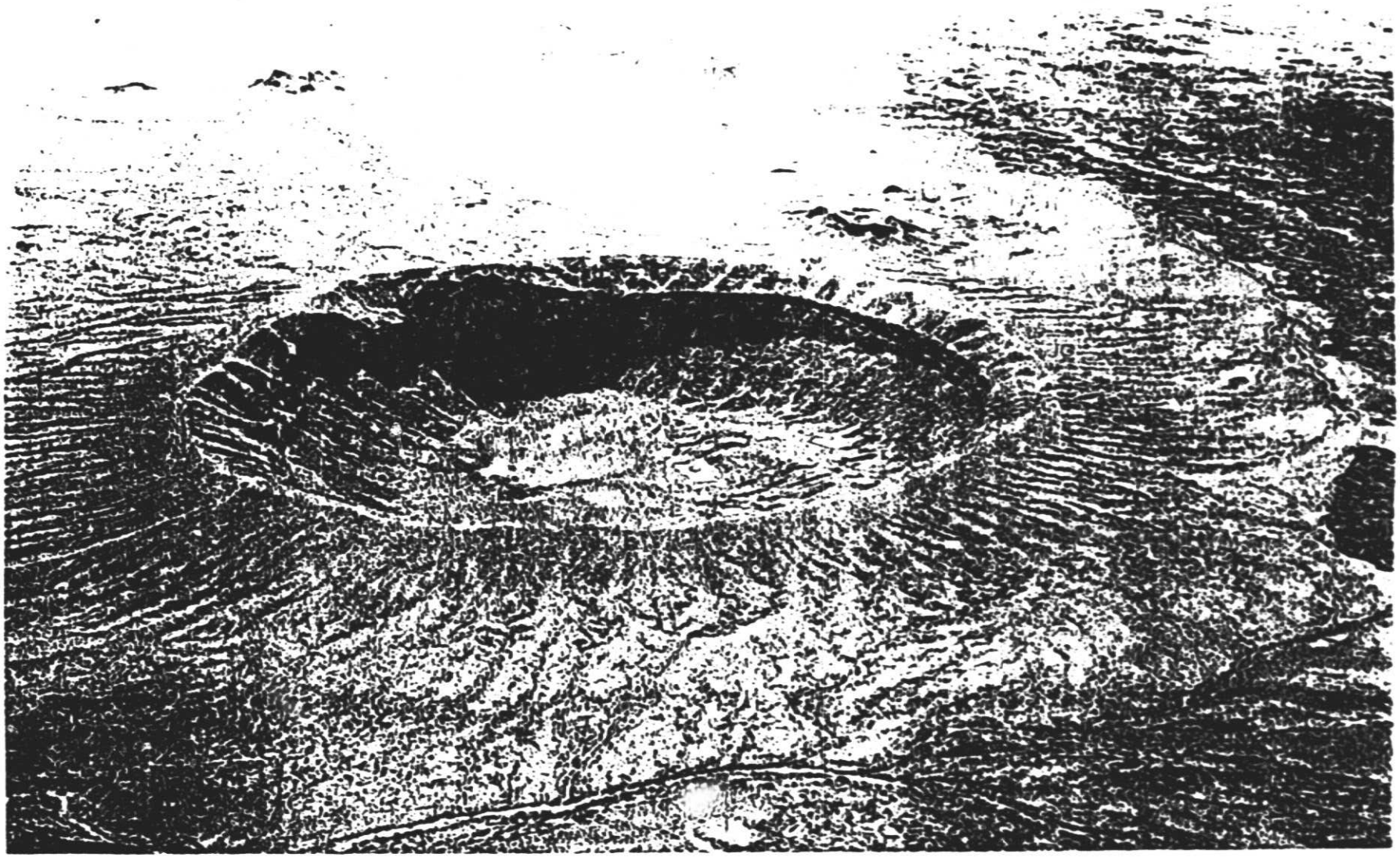

Greeley et al. Fig. 14b

Top

Greeley et al. fig. 14C

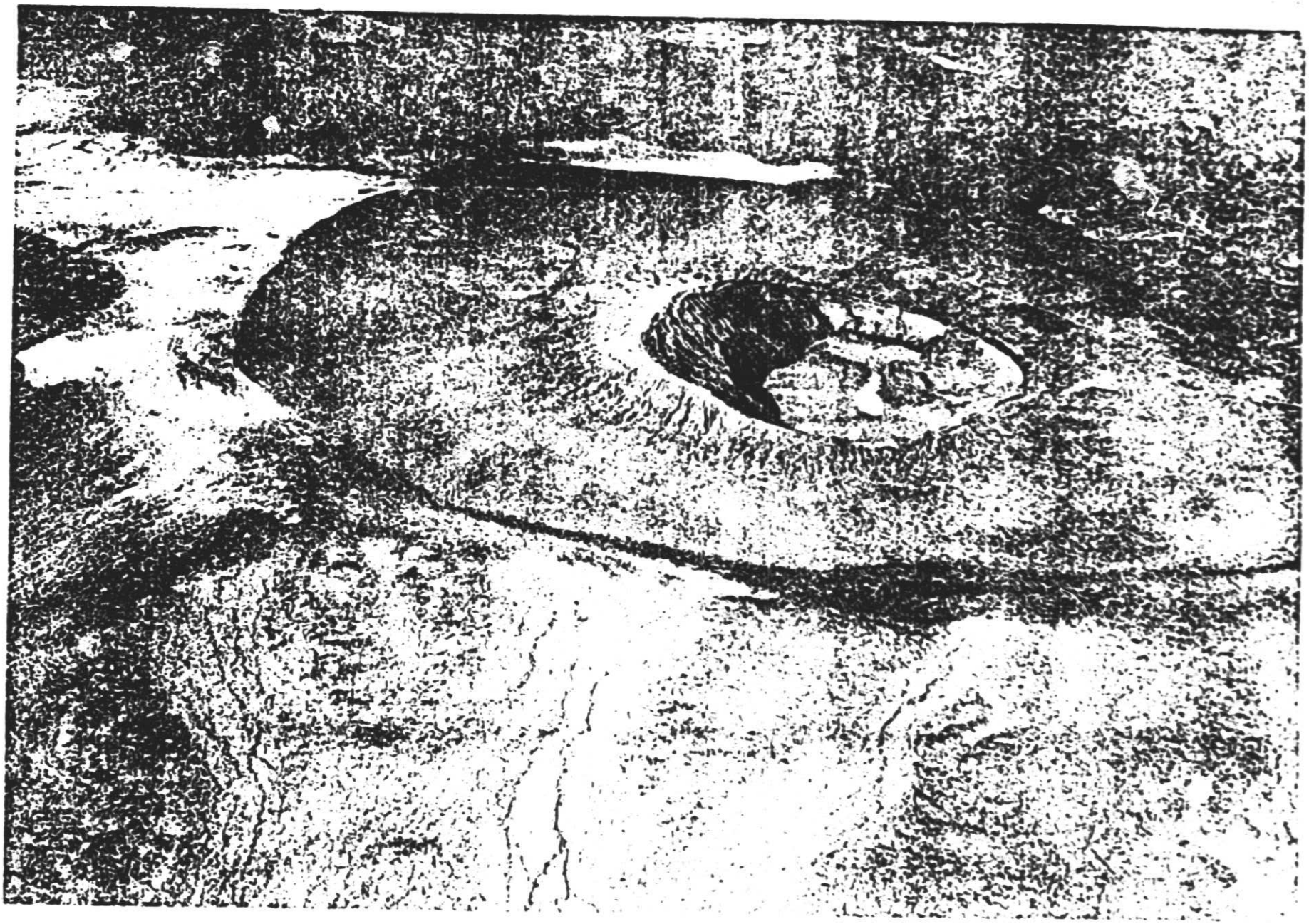

Greeley et al. Fig. 14d

Top

Greeley et al. Fig. 14e

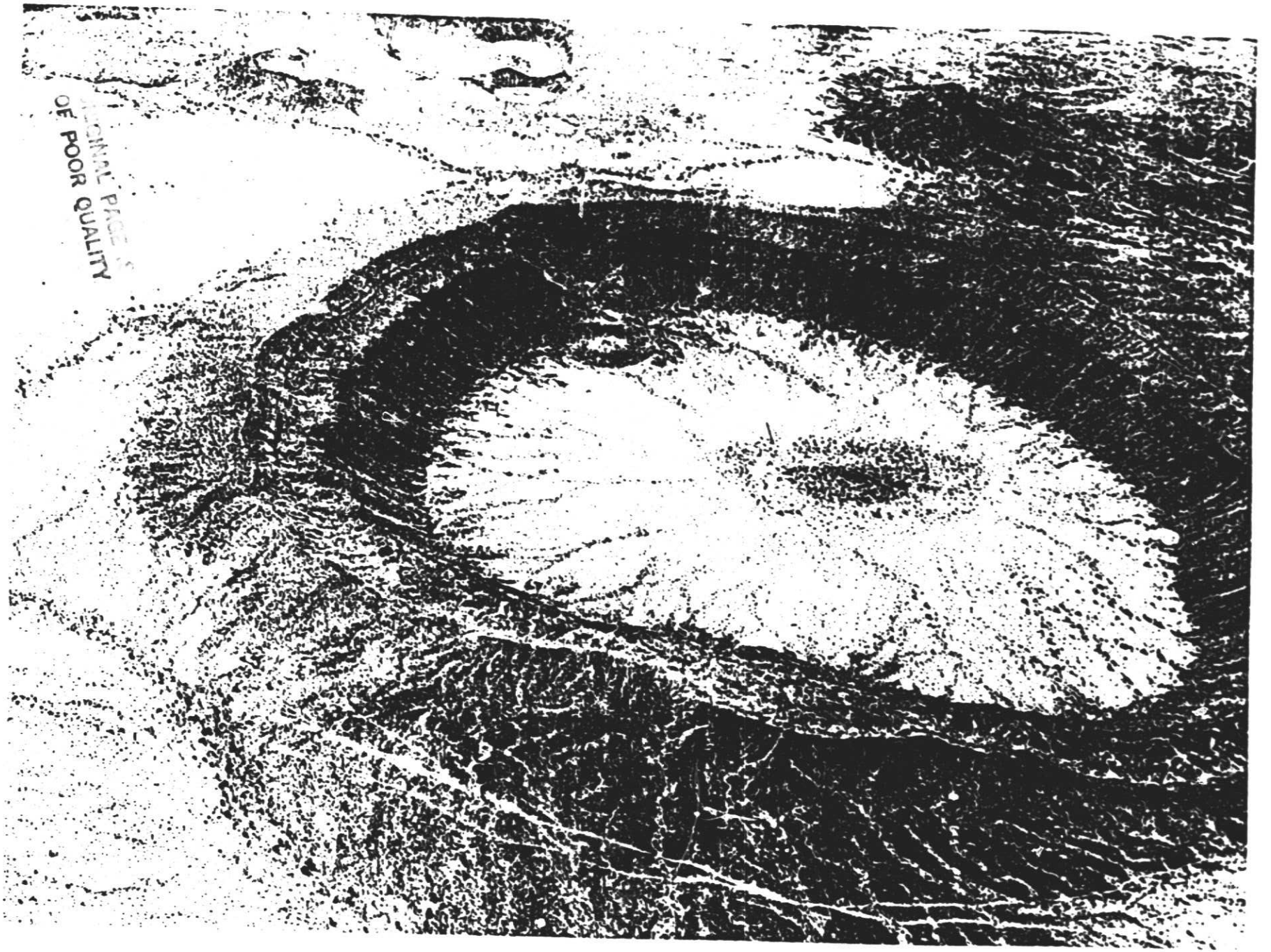

Greeley et al. Fig. 14f

Greeley et al. Fig. 14g

Greeley et al. Fig. 14h

Top

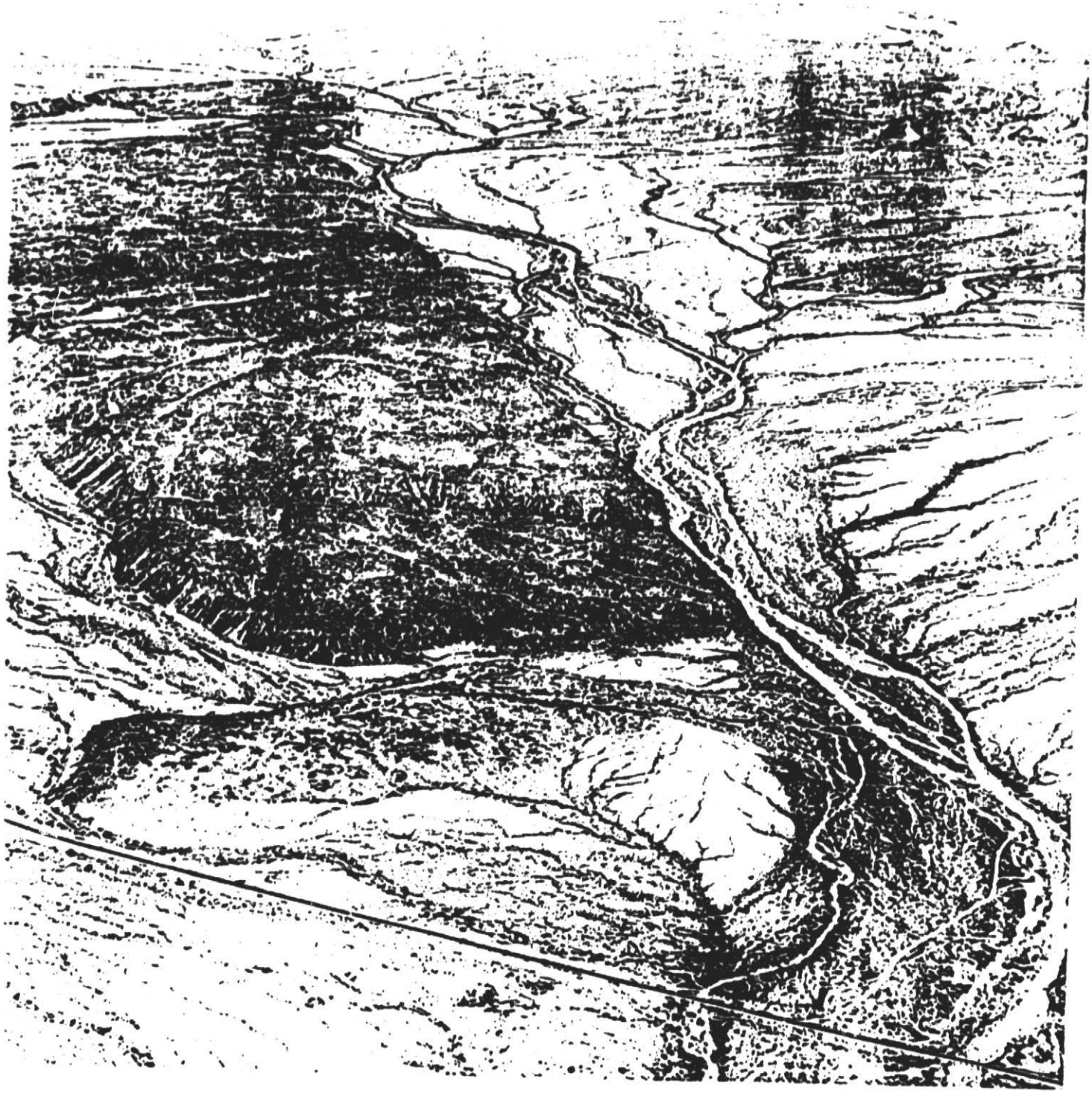

Greeley et al. Fig. 15

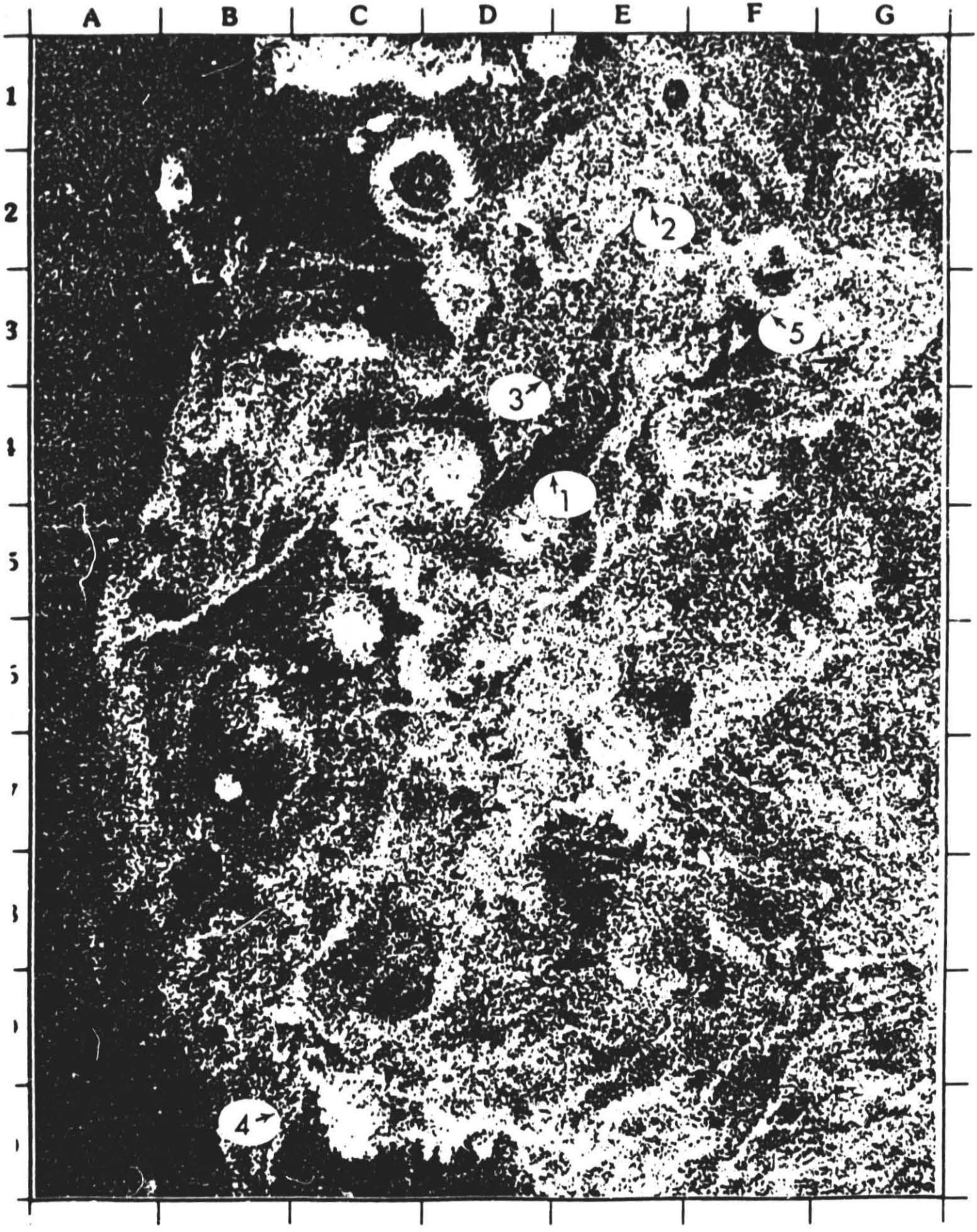

Top

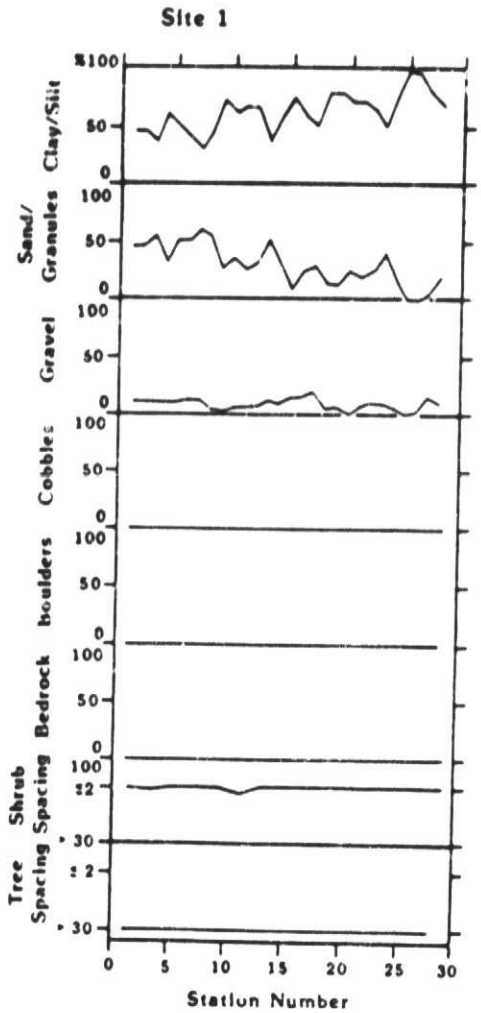

Greeley et al. Fig. 17

ORIGINAL PAGE IS
OF POOR QUALITY

Greeley et al. Fig. 18

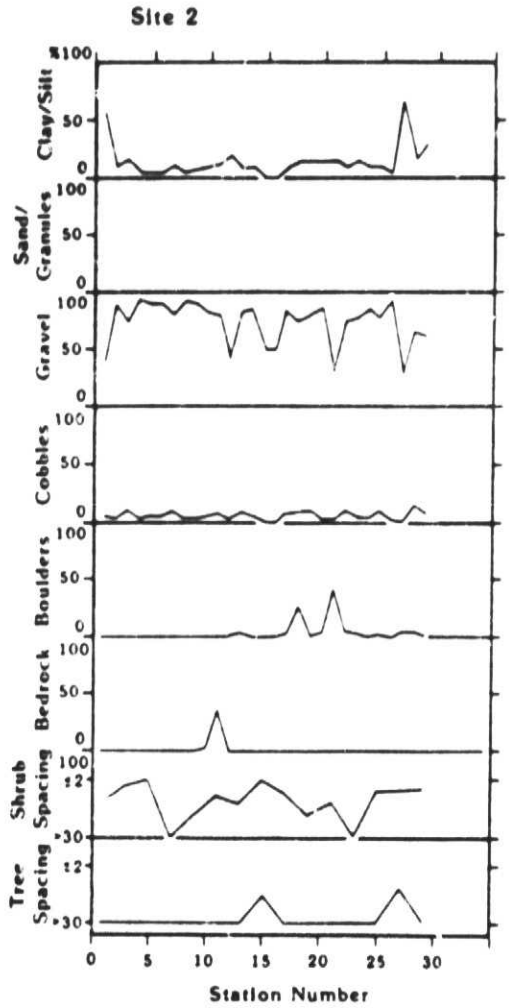

Greeley et al. Fig. 19

Greeley et al. Fig. 20a

Greeley et al. Fig. 20b

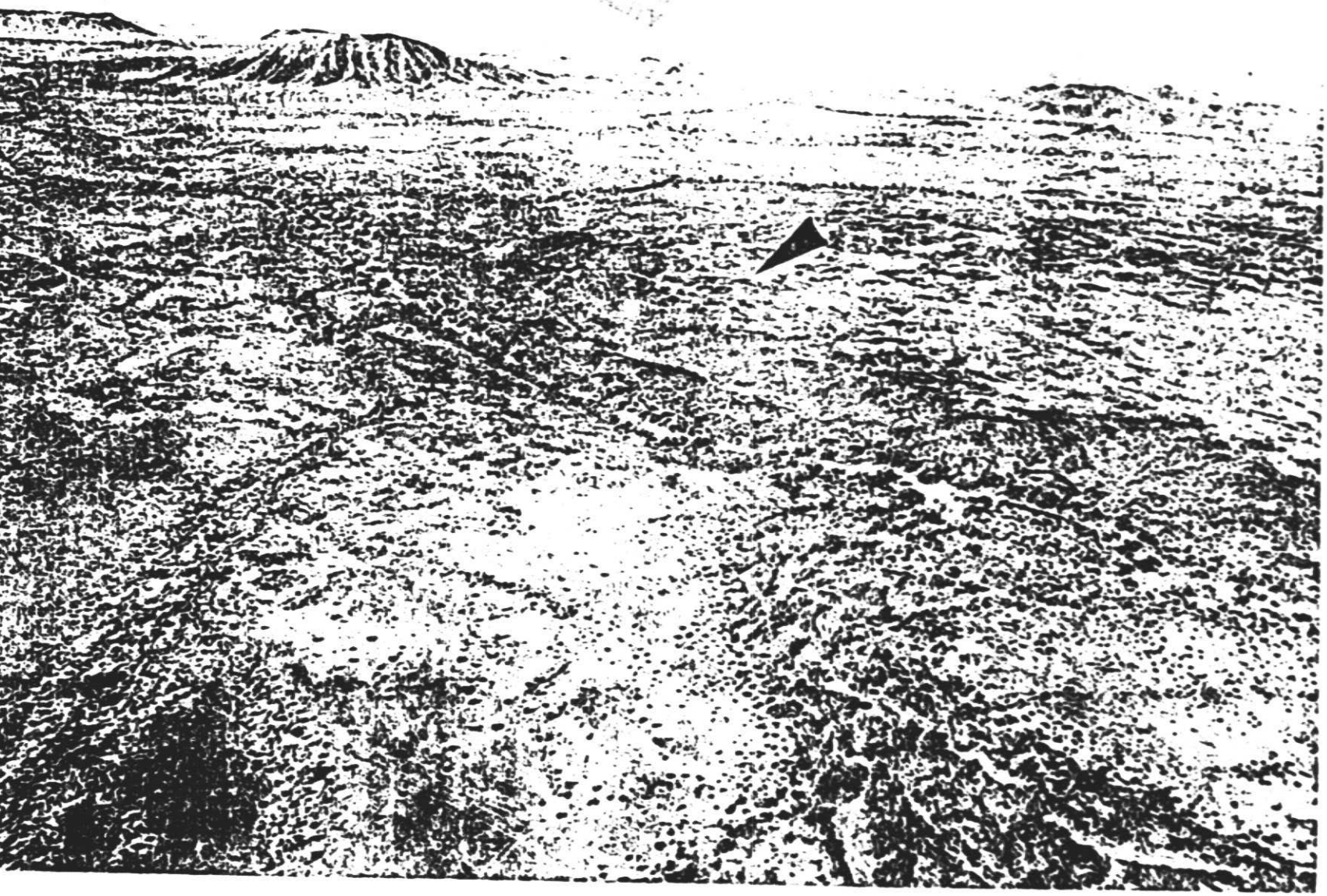

ley et al. Fig. 21a

Greeley et al. Fig. 21b

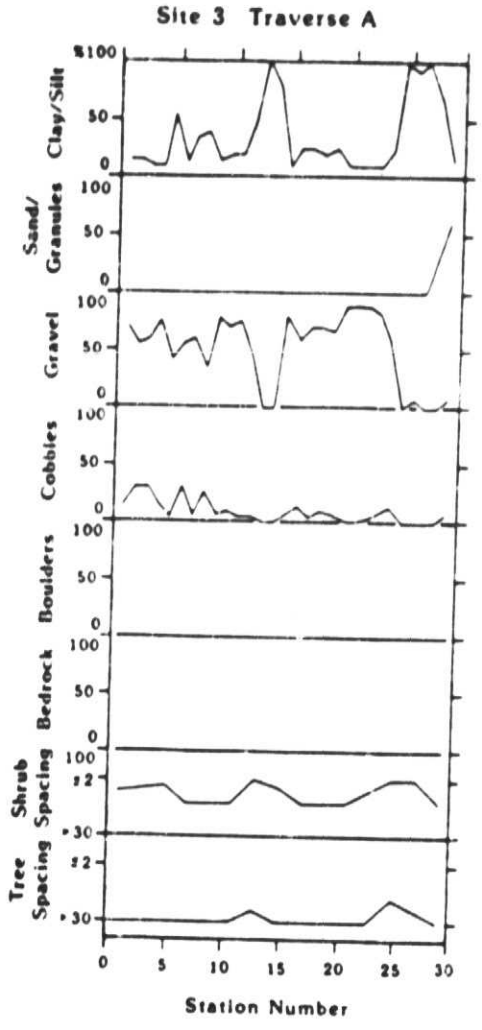

Greeley et al. Fig. 22a

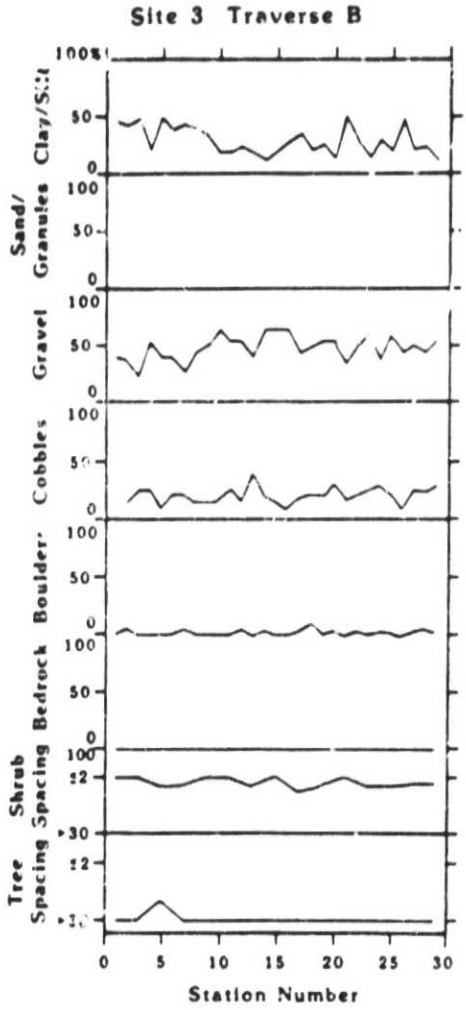

Greeley et al. Fig. 22b

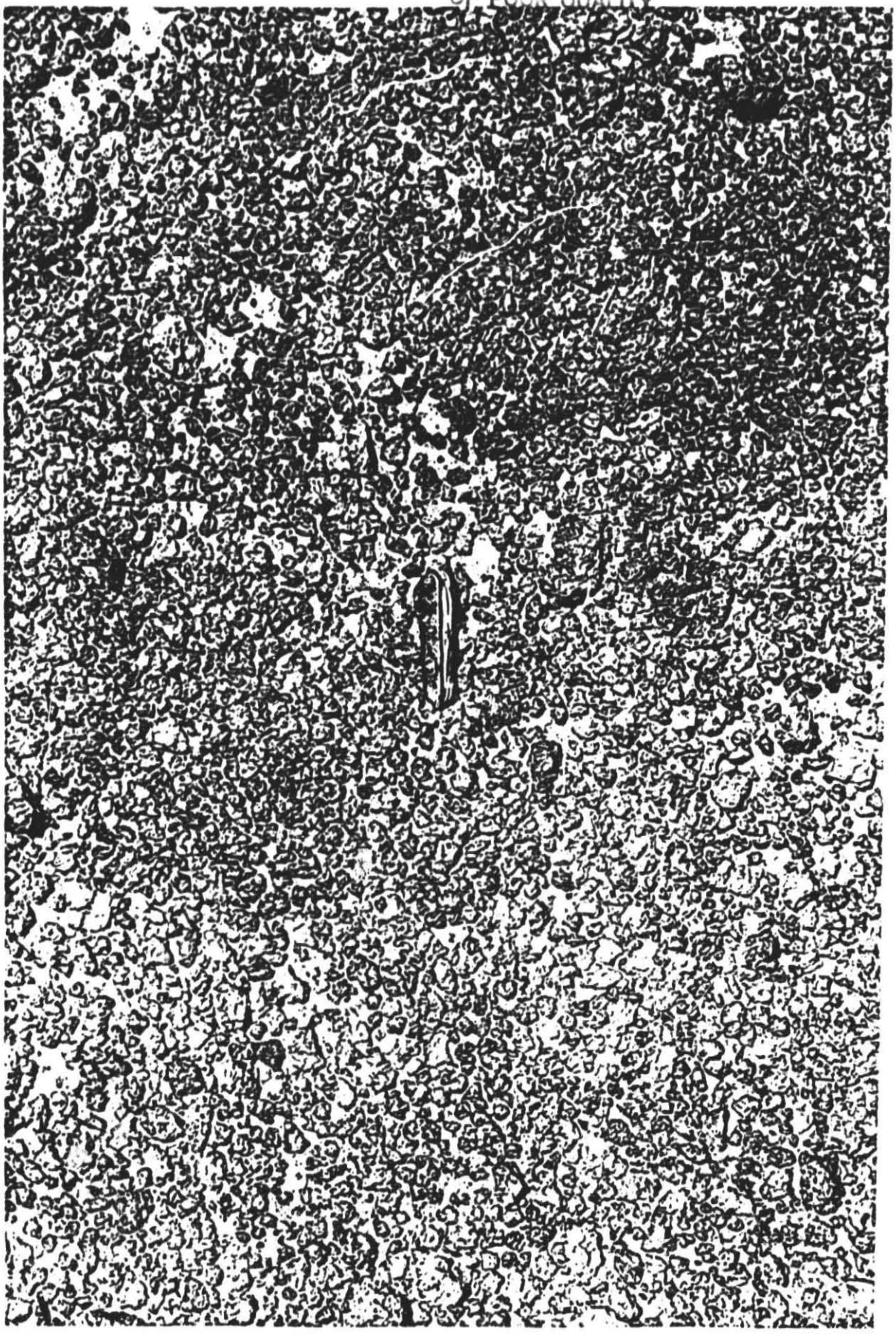

Graedel et al. Fig. 23a

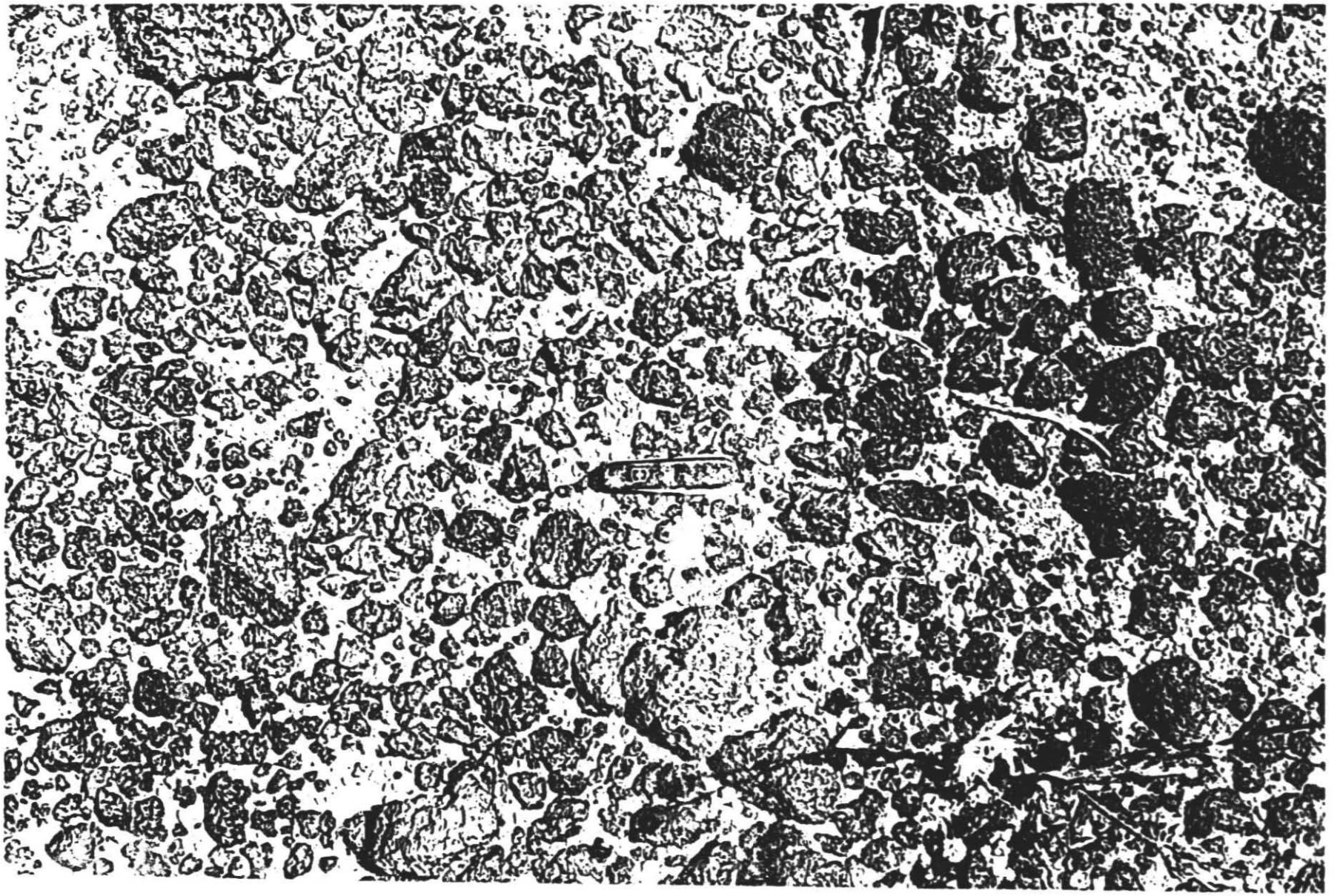

Greeley et al. Fig. 23b

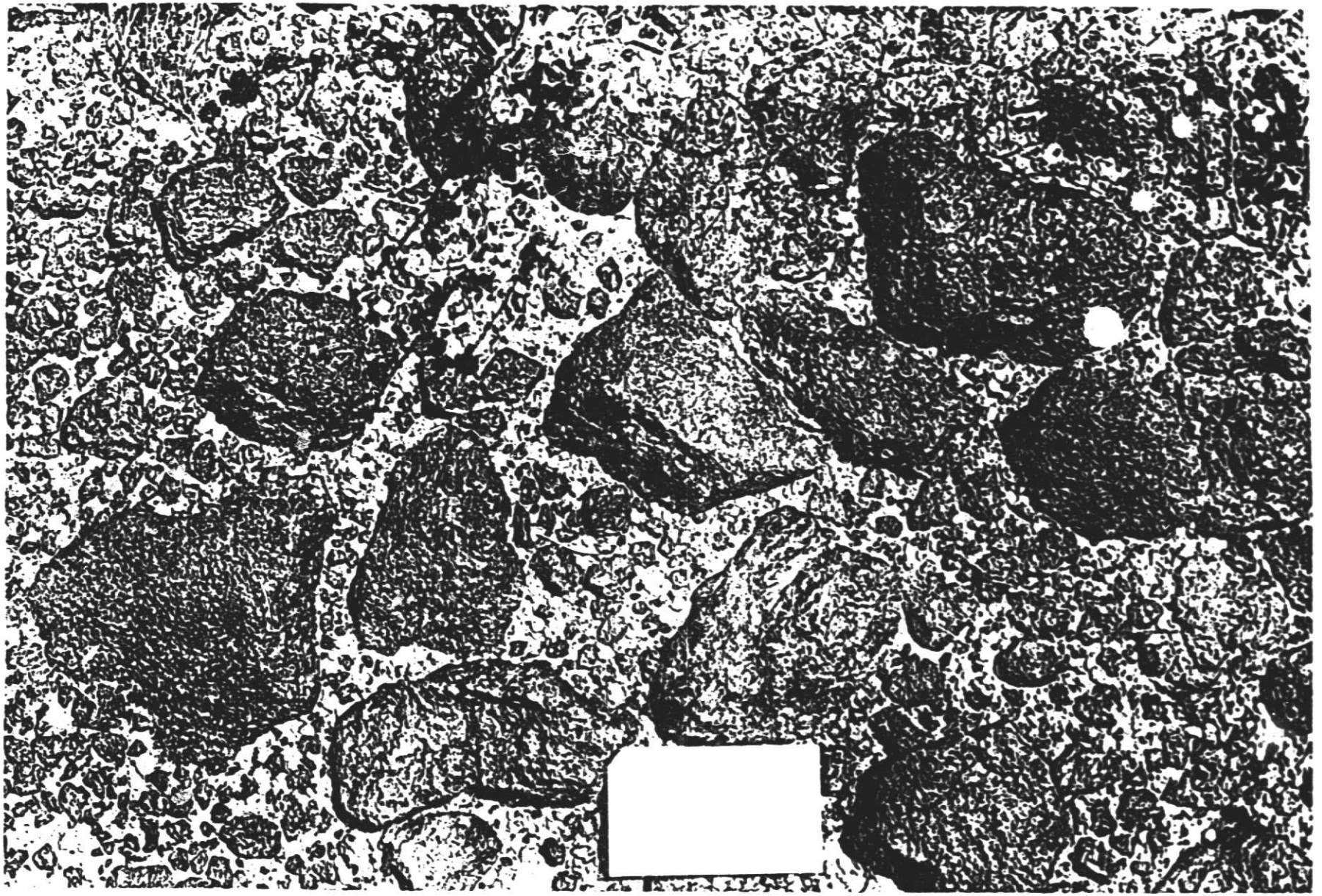

Greeley et al. Fig. 23d

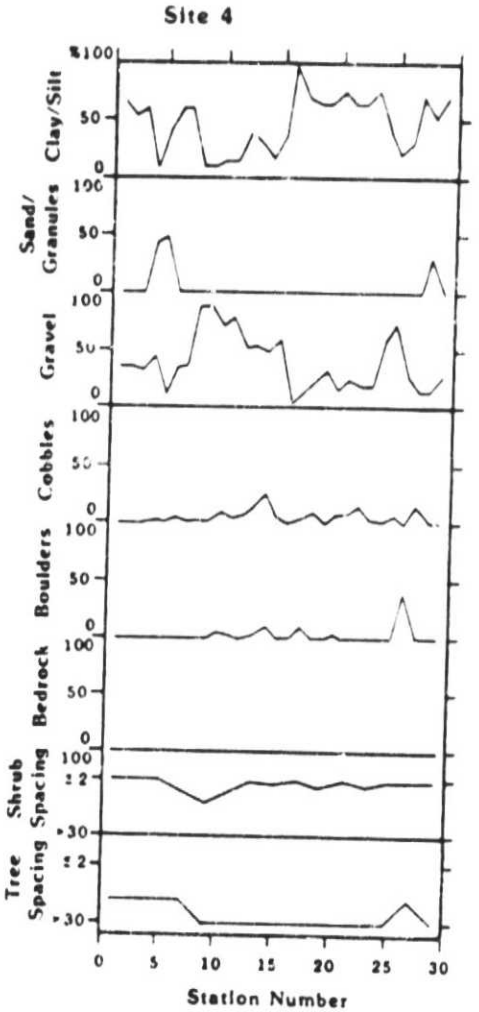

Greeley et al. Fig. 24

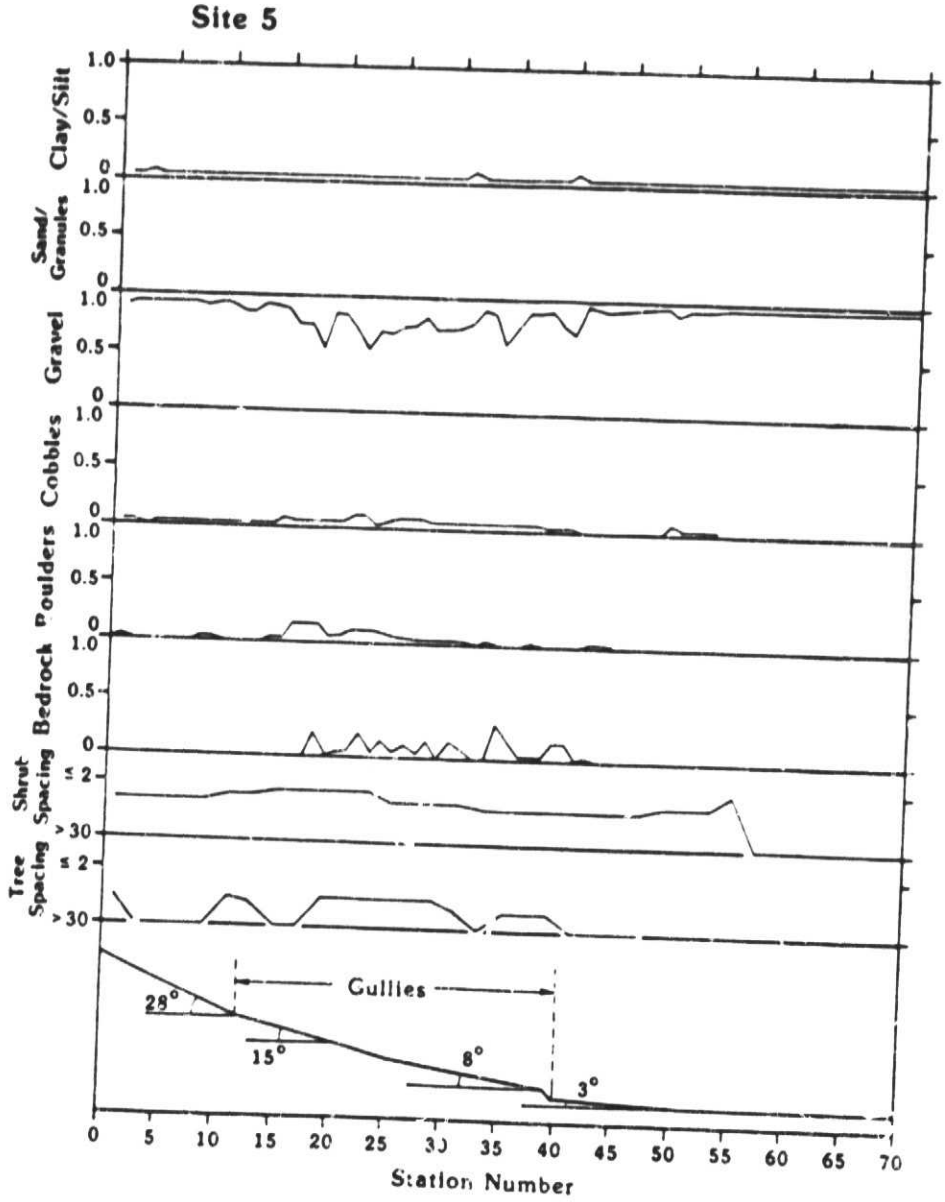

Greeley et al. Fig. 25

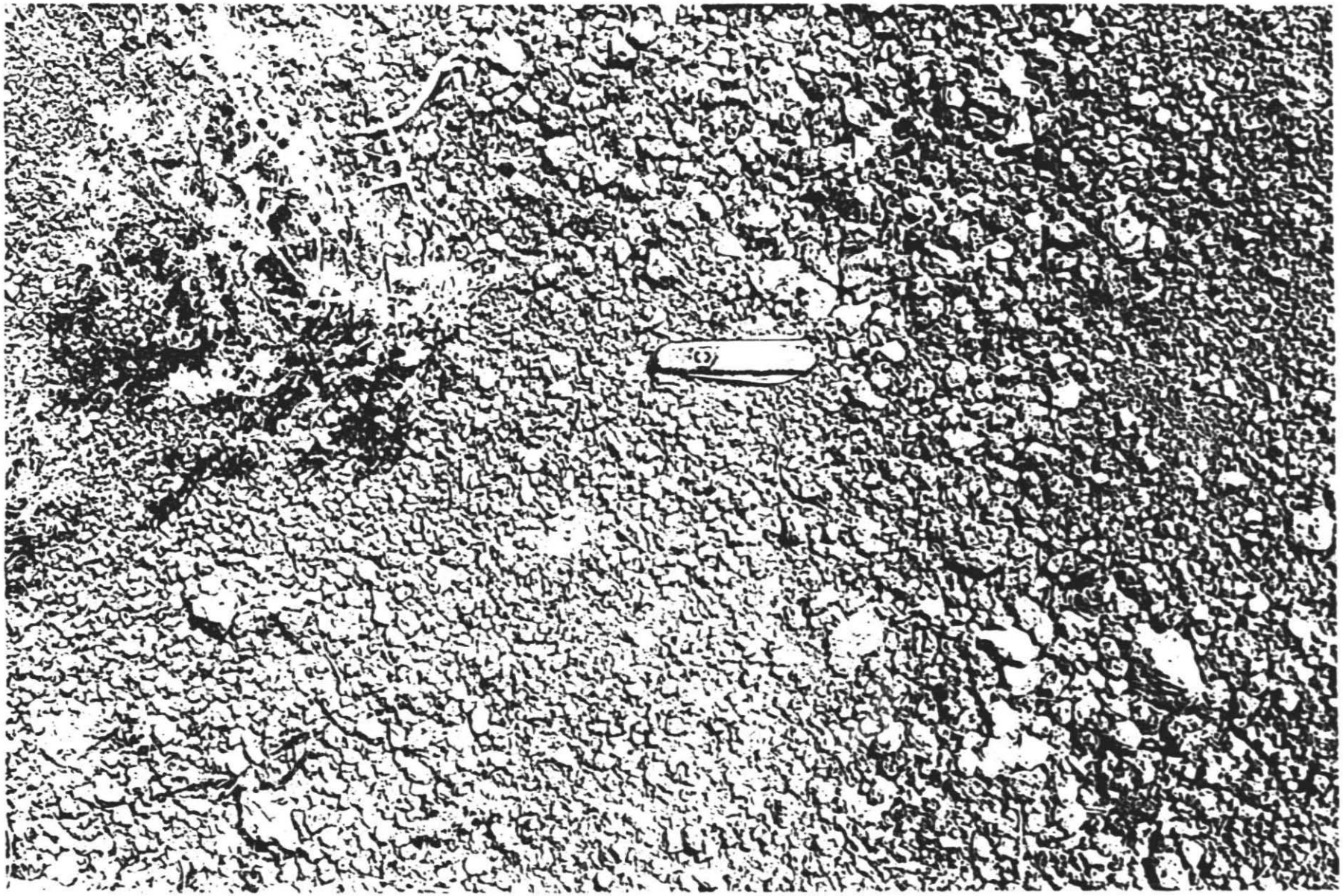

Greeley et al. Fig. 26a

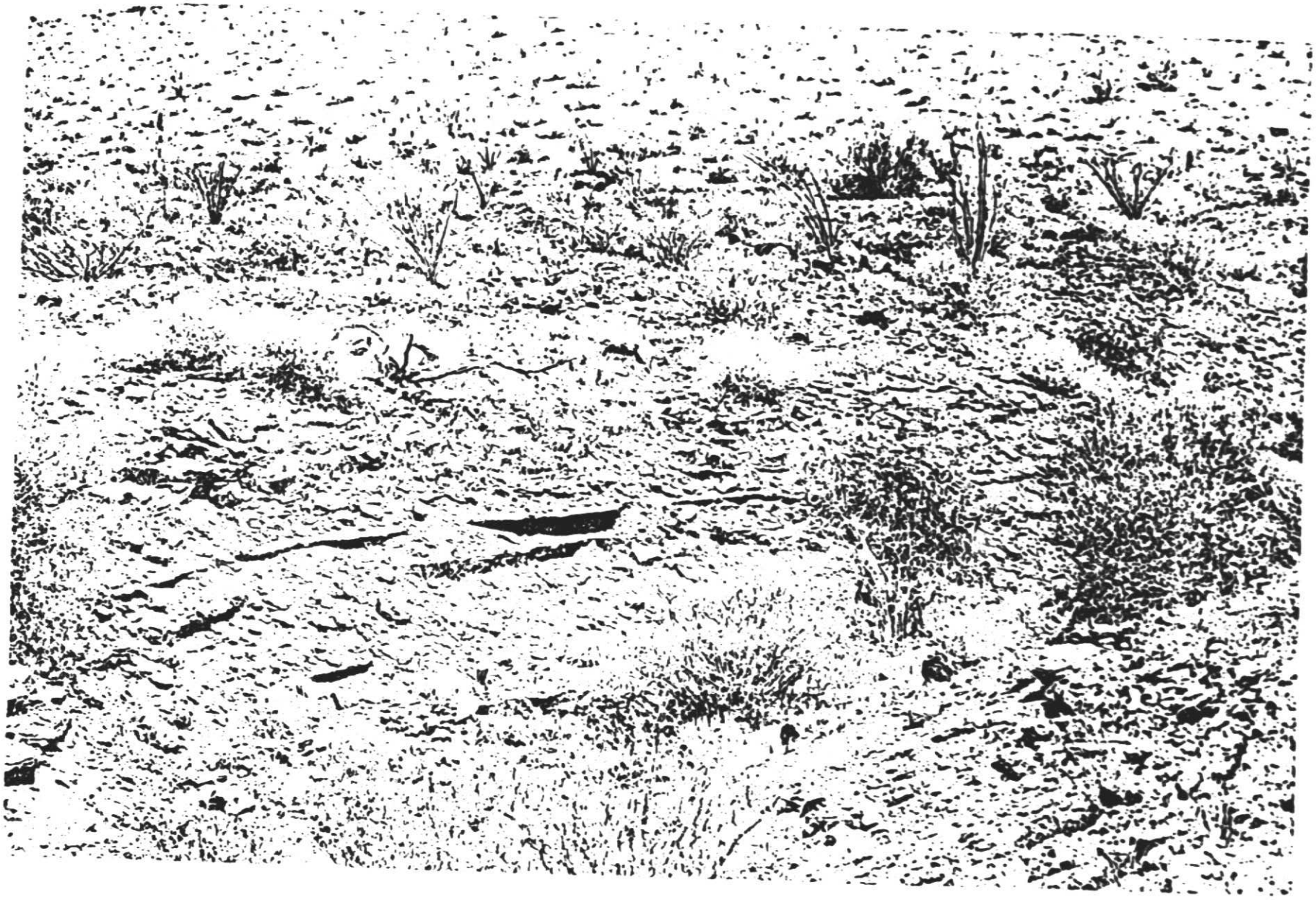

Greeley et al. Fig. 26b

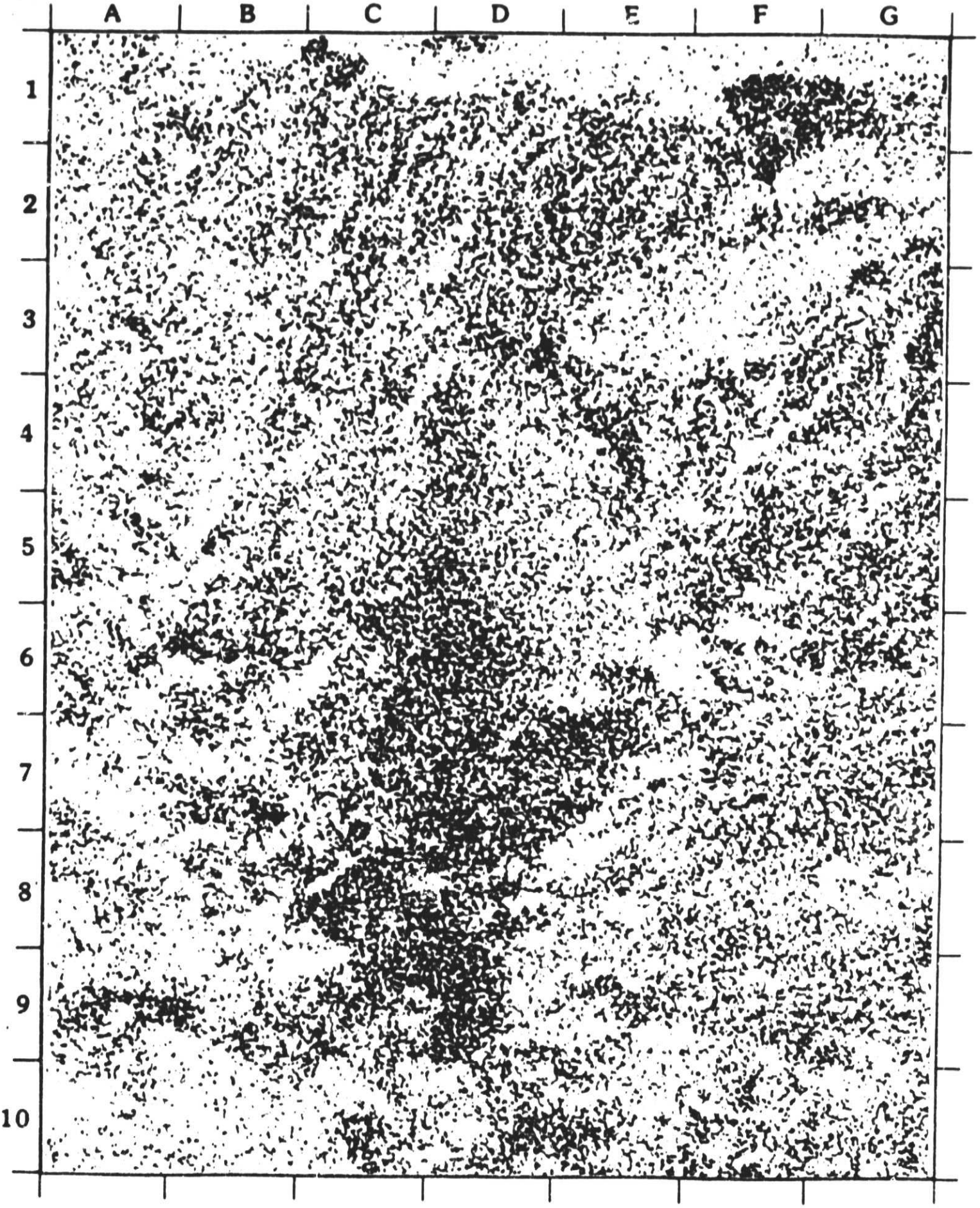
A
B
C
D
E
F
G
1
2
3
4
5
6
7
8
9
10

Greeley et al.
Fig. 28a

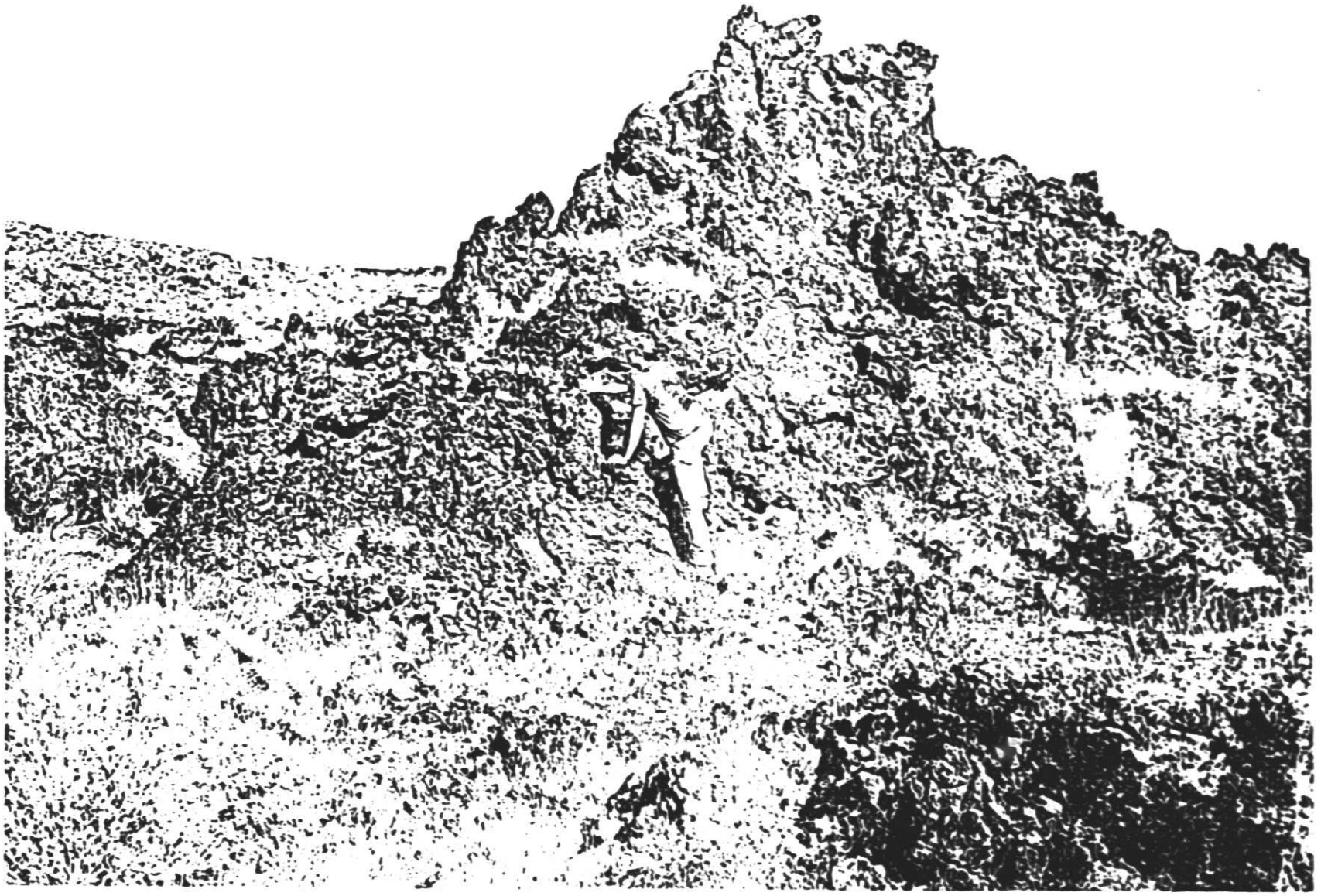

Greeley et al. Fig. 28 b

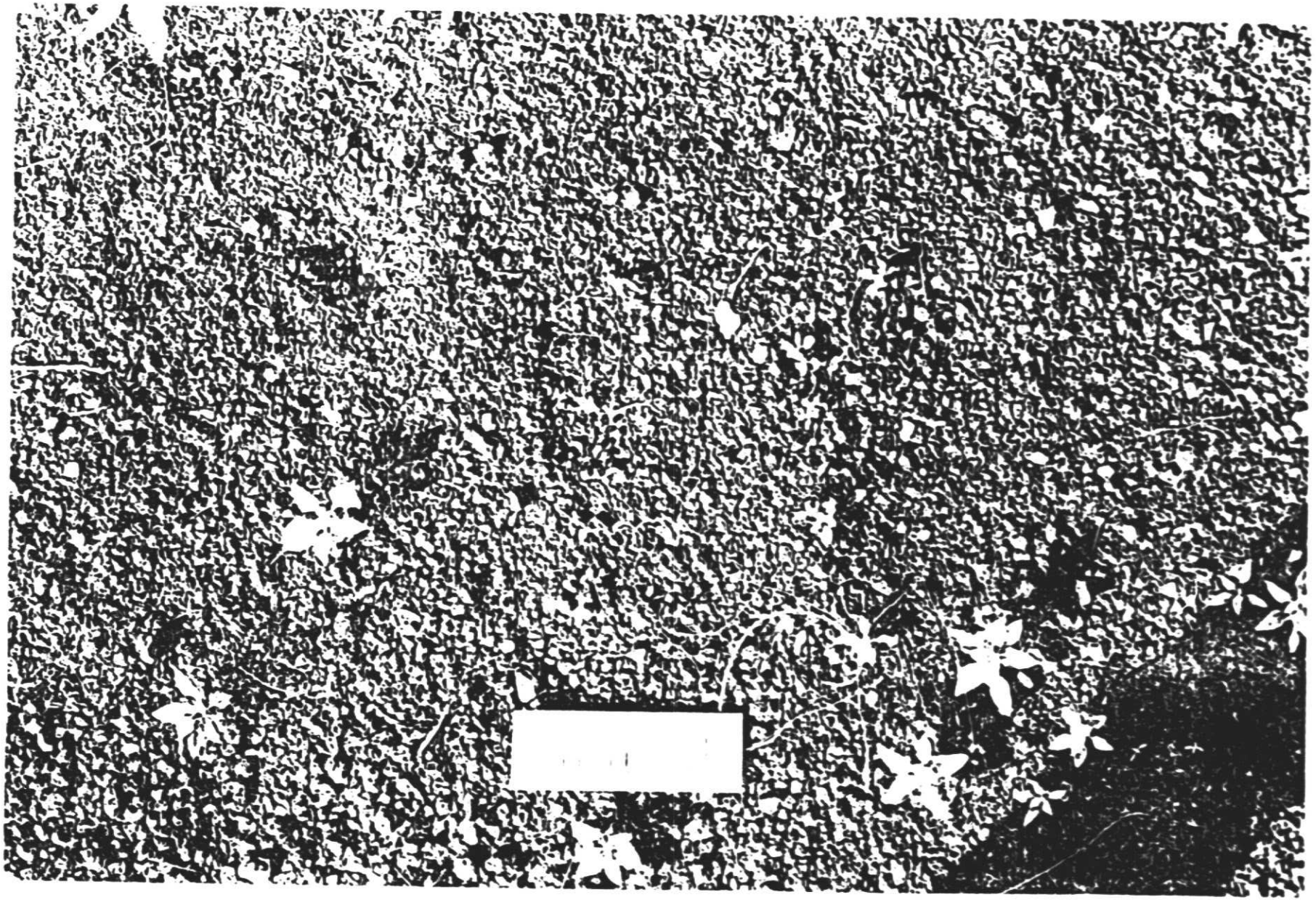

Greeley et al. Fig. 29a

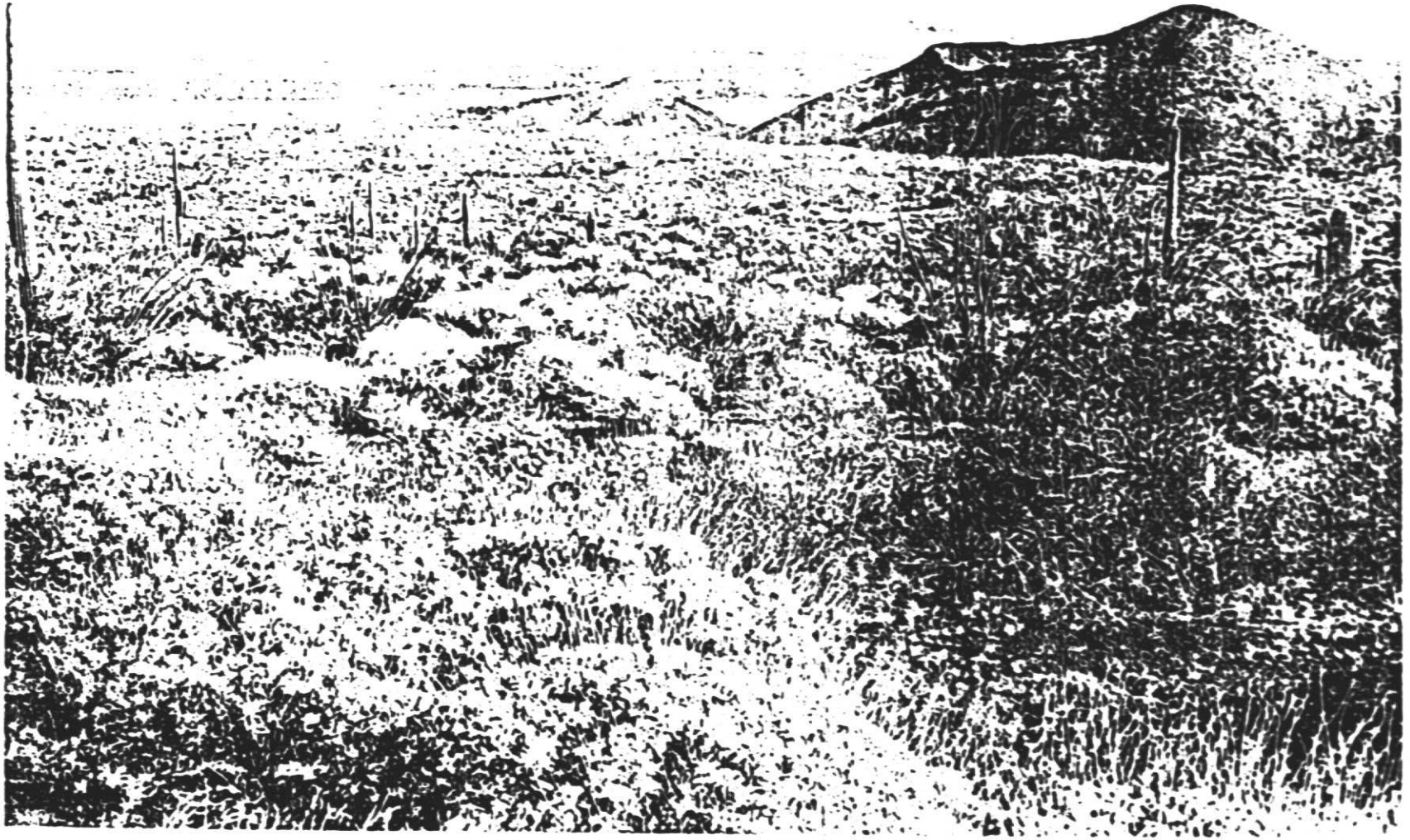

Greeley et al. Fig. 29b

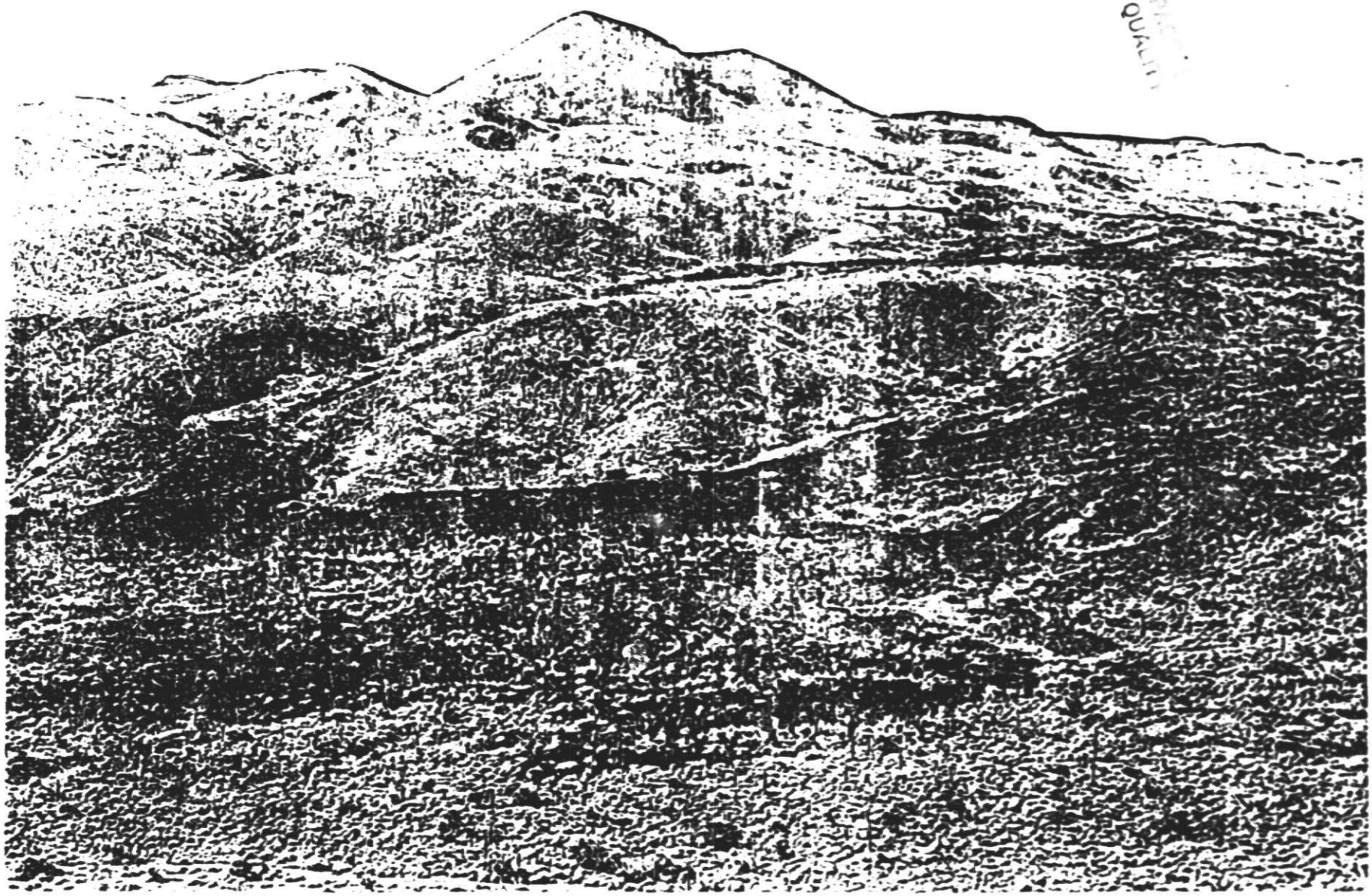

Greeley et al. Fig. 30a

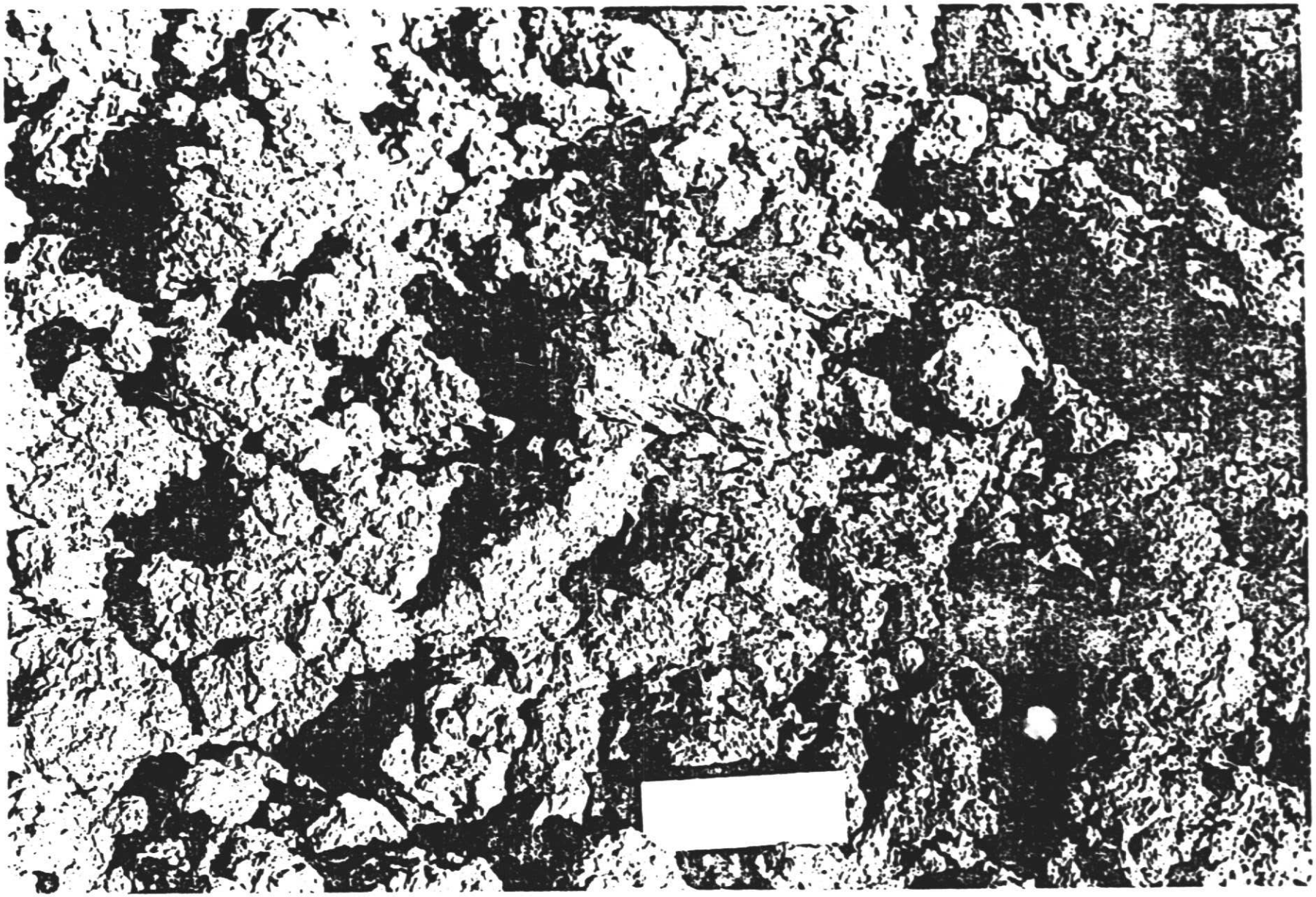

Greeley et al. Fig. 30b

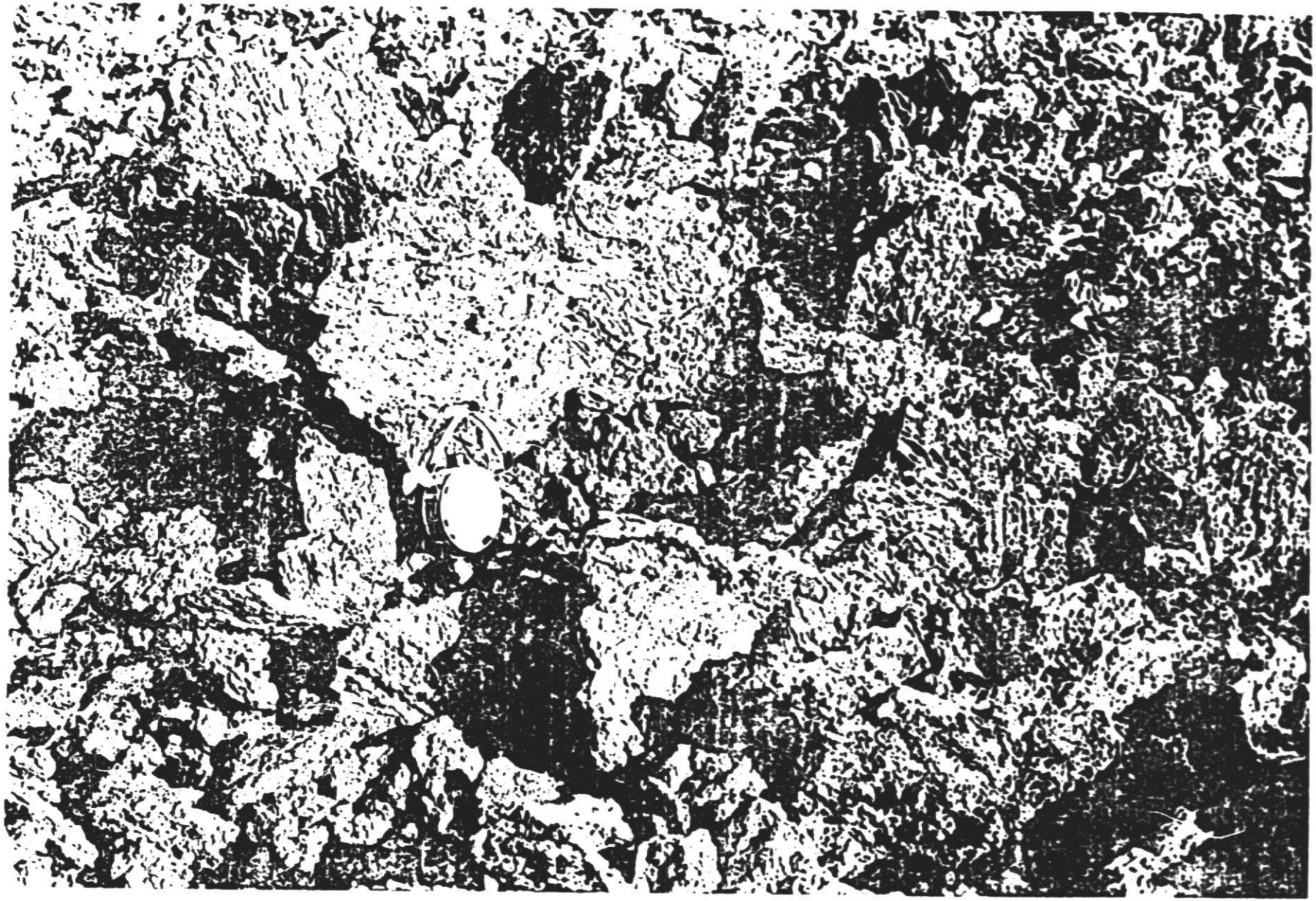

Greeley et al. Fig. 30C

Greeley et al. Fig 31a

Greeley et al. Fig. 31b

Greeley et al. Fig. 31C

Greeley et al. Fig. 32a

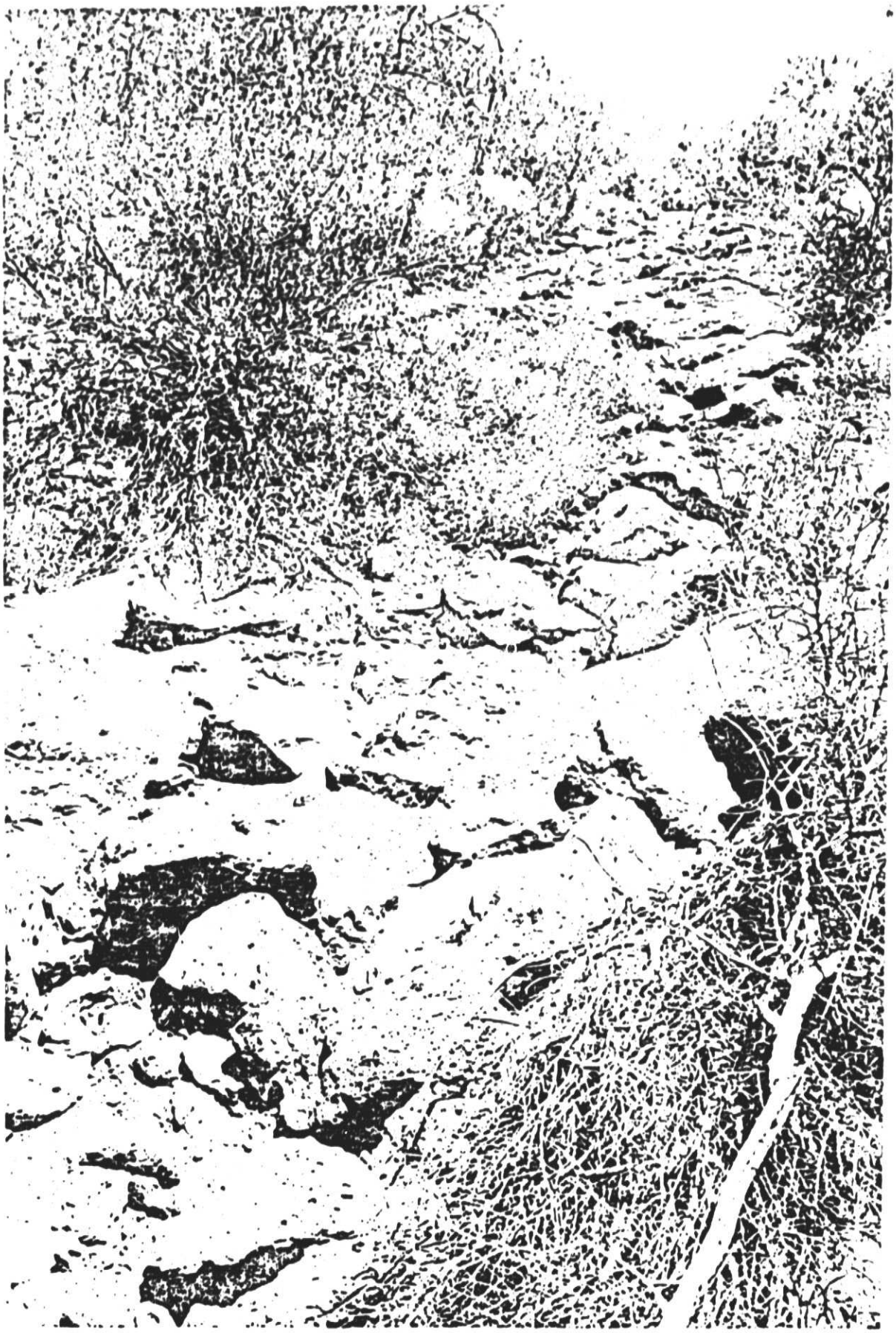

Greeley et al. Fig. 32b

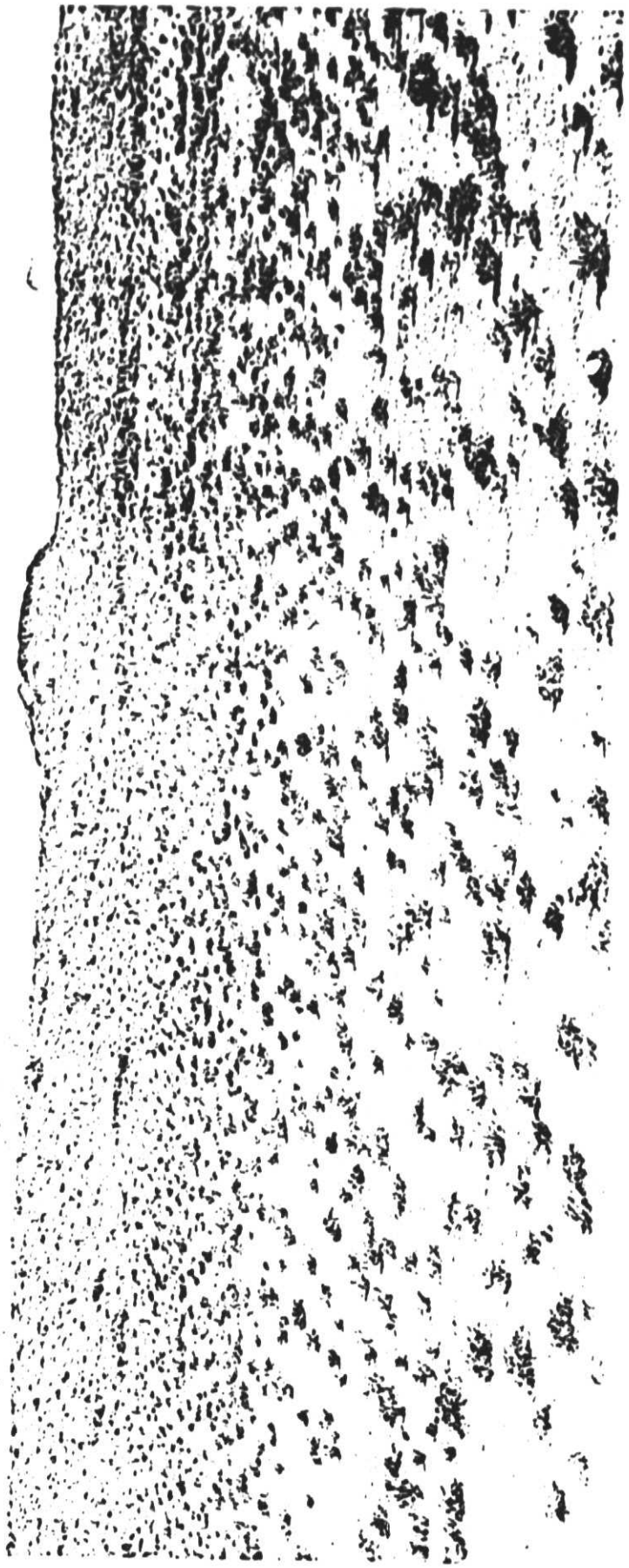

Greeley et al. Fig. 33a

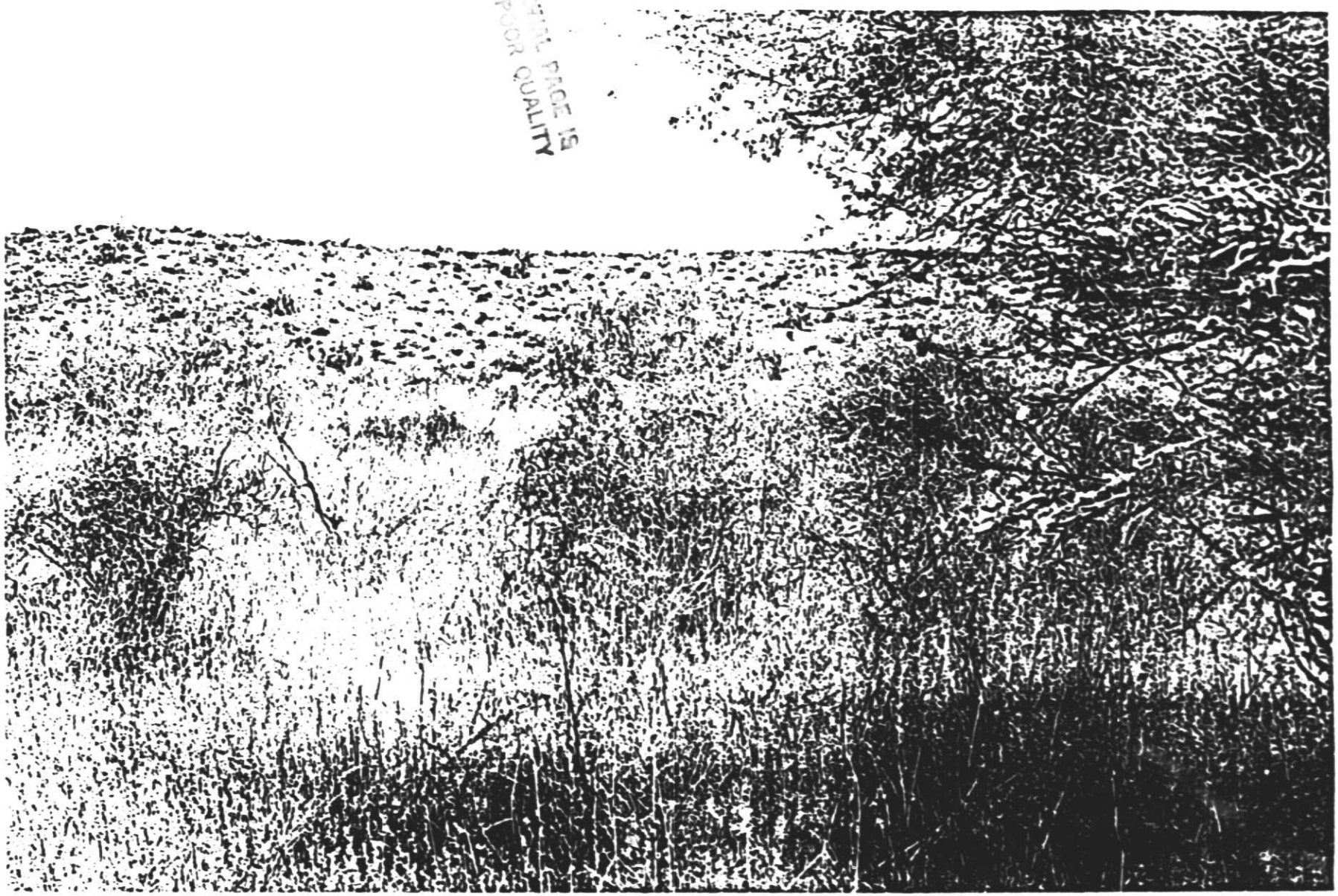

Greeley et al. Fig. 33b